How caged motion in the contact layer enhances thermal tunneling across a liquid/solid interface

Hiroki Kaifu and Sandra M. Troian*
California Institute of Technology, T. J. Watson Sr. Laboratories of Applied Physics, MC 128-95, Pasadena, California 91125, USA

Artem I. Baskin
NASA Ames Research Center, Moffett Field, California 94035, USA

(Received 30 December 2023; accepted 2 July 2024; published 31 July 2024)

Ever more powerful and densely packed chips for applications like cryptocurrency mining and artificial intelligence generate such enormous heat fluxes that designers are pivoting from gas to liquid cooling to forestall damage from thermal runaway. Even with optimal flow patterns, however, the intrinsic thermal boundary resistance at the liquid/solid (L/S) interface poses an additional source of thermal impedance. There is a lingering misconception in the field that the higher the liquid contact density, the more frequent the L/S collision rate and the smaller the thermal slip length. Here we present an insightful counterexample based on nonequilibrium molecular dynamics simulations of a simple liquid confined between two face centered cubic crystals at different temperatures aligned with the [001], [011] or [111] facet plane. Measurements of various static and dynamic quantities of the contact layer reveal the ways in which long-range order, anisotropy of the L/S potential, and correlated motion act to reduce thermal boundary resistance. Systems with the smallest thermal slip length exhibit two distinct features: 2D caged motion with stringlike alignment of liquid particles, unlike that observed in glassy systems, and larger nonergodicity parameter with shorter, not longer, caging times. This trapping and release mechanism suggests a paradigm for the design of L/S interfaces to maximize thermal exchange across a classical L/S interface.

DOI: 10.1103/PhysRevResearch.6.033123

I. INTRODUCTION

The question of how interfacial properties can be tuned to enhance thermal flux across a liquid/solid (L/S) interface is an old one dating back more than half a century. A satisfactory answer remains out of reach in part because accurate models for phonon propagation in liquids are still being developed. This question, however, has taken on renewed interest due to a pressing technological problem related to ever smaller and increasingly more powerful computing chips. Central processing and graphics processing units specifically designed for computations involving artificial intelligence and cryptocurrency mining run so hot and for so long that cooling issues now comprise about 40% of the cost of operating a data center [1]. And despite that chip designers have pivoted from gas to liquid cooling, the march toward even smaller, more powerful, and more tightly packed components as in recent 3D integrated chips has created a design bottleneck associated with challenges in extracting waste heat [2].

Given the thermal constraints imposed by tight spatial integration, there is a clear need for innovative designs which can position the cooling element as close as possible to the active hot components. One solution is precision cooling in which a liquid cooled chassis and delivery manifold based on a microfluidic network funnel the flow of the dielectric coolant directly to hotter components [3]. Another solution is direct immersion cooling in which electronic components are directly submerged in a bath of static or circulating dielectric liquid [4,5]. There now exists a growing industry focused exclusively on optimizing the flow pattern and speed throughout the embedded network for rapid and efficient extraction of heat from heterogeneous components in electronic devices [2].

There exists an additional source of thermal impedance associated with the L/S interface by virtue of the fact that phonons partially transmit and reflect at the boundary separating the two media. At nanoscale dimensions, this thermal boundary resistance (TBR) can take on values comparable to the thermal resistance of the bulk solid or liquid and therefore cannot be ignored. The design for the IBM nanosheet cooled by liquid nitrogen contains more than fifty billion transistors on a chip the size of a fingernail [6]. The area per transistor is roughly 10^{-11} cm^2 (or, equivalently, 30 nm per edge). At these dimensions, expelling waste heat at high flux through the interface requires better molecular-scale understanding of interfacial thermal exchange.

For two materials in contact subject to a constant thermal flux J_z propagating across the separating boundary

*Contact author: stroian@caltech.edu; http://www.troian.caltech.edu

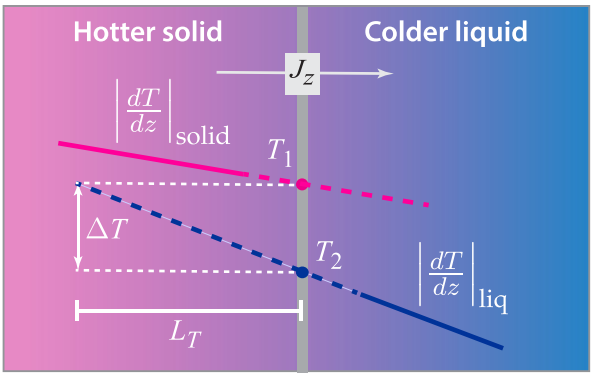

FIG. 1. Diagram illustrating the thermal slip length $L_T = (T_1 - T_2)/|dT/dz|_{\text{liq}}$, where $\Delta T = T_1 - T_2 > 0$.

and whose surface temperatures maintain a thermal jump $\Delta T = T_1 - T_2 > 0$, the TBR is defined as

$$\mathcal{R} = \frac{\Delta T}{J_z}. \tag{1}$$

For any medium governed by Fourier's law, the thermal flux is prescribed by the well-known relation

$$J_z = k(T)\left|\frac{dT}{dz}\right|, \tag{2}$$

where dT/dz is the local thermal gradient and $k(T)$ the local thermal conductivity. For Fourier conductors, k depends on temperature but cannot depend on dT/dz or higher derivatives of temperature. In systems at the steady state, the thermal flux must be everywhere constant.

Thermal jumps were first measured in quantum systems using superfluid helium in contact with different metal surfaces [7]; later studies demonstrated the same phenomenon at a classical L/S interface. Thermal impedance at a L/S interface is normally quantified by the thermal slip length

$$L_T = \frac{\Delta T}{|dT/dz|_{\text{liq}}}, \tag{3}$$

which is simply the thermal jump across the interface normalized by the thermal gradient $|dT/dz|_{\text{liq}}$ in the quiescent liquid interior. As illustrated in Fig. 1, L_T is the virtual distance within the solid where extrapolation of the slope $|dT/dz|_{\text{liq}}$ recovers the temperature T_1.

Researchers continue to improve the accuracy and sensitivity of instrumentation for measuring $\mathcal{R}$ and L_T at solid/solid [8] and L/S interfaces [9]. However, techniques still lack the desired spatiotemporal resolution or thermal source penetration depth required [8]. Researchers therefore continue to rely on nonequilibrium molecular dynamics (NEMD) simulations for molecular level understanding of thermal exchange across the L/S barrier, especially given favorable comparison between experiment and simulation for many systems [9,10]. Fundamental studies based on spherically symmetric, two-body interactions between simple neutral particles utilize the Lennard-Jones (LJ) pair potential, known to generate highly accurate predictions of the thermophysical properties of argon and other substances in the gaseous, liquid, and solid phases. Since the LJ potential U_{LJ} scales as $\varepsilon U_{\text{LJ}}(|\vec{r}|/\sigma)$, where ε is the interparticle interaction energy, $|\vec{r}|$ the particle separation distance, and σ the approximate repulsive distance or effective particle diameter, the principle of corresponding states [11] allows many other liquids and solids to be modeled accurately by different choices ε and σ [11,12].

NEMD studies of a quiescent liquid layer between two solids at different temperatures have long confirmed the validity of Fourier's law at gas-liquid coexistence all the way to the freezing point [13]. This confirmation established NEMD as a valid tool for exploring transport phenomena from the macroscopic to molecular scale dimensions. There is now a vast literature detailing correlations uncovered between the thermal slip length (or $\mathcal{R}$ or thermal boundary conductance) and various system parameters including the L/S interaction energy [14–20], liquid pressure [21,22], solid surface temperature [23,24], crystal symmetry [25,26], solid surface roughness [20], spring stiffness controlling solid wall particle vibrations [27], thickness of the liquid and solid layer [28,29], and the degree of liquid layering near a solid surface, initially reported in equilibrium systems [30–32].

The degree of liquid layering has been assumed to play an important role in thermal transfer across a L/S interface and, as a result, special attention has been paid to the so-called contact density ρ_c, namely, the density of the first layer of liquid near the solid. As is customary, we shall refer to this layer as the *contact layer*, the main focus of our paper. Early studies [16,17] and many since then have shown that as the L/S bonding strength ε_{LS} increases, the thermal boundary resistance decreases. This effect has been attributed to higher contact density, which facilitates more frequent collisions between liquid and solid particles, thereby enhancing thermal exchange [33,34]. In simulations, the contact density ρ_c can be increased by lowering temperature, increasing liquid pressure or using denser model liquids. All these effects appear to reduce TBR [22,35,36]. NEMD studies of water against solid silicon have also demonstrated strong association between smaller TBR and thinner depletion layer thickness [26,34,37]. In sum, these findings have been used to support the view that under similar conditions, a higher contact density results in a smaller thermal slip length.

In this paper, we present a compelling counterexample which demonstrates that under similar thermal conditions, the L/S interface with the smallest contact density incurs the highest thermal flux and smallest thermal slip length. This NEMD study is based on a simple liquid confined between two solids held at different temperatures, which are identically oriented along one of three facets of a face centered cubic (FCC) lattice for different values of L/S bonding strength and different temperature. The results highlight the critical role of the liquid contact layer and how long-range order, anisotropy of the L/S potential, and correlated motion combine to reduce the thermal impedance to minimize the thermal slip length. The computational details and statistical measures used to quantify structure and motion in the contact layer are outlined in Sec. II. The results in Sec. III illustrate the influence of L/S interaction energy, crystal facet, and layer temperature, and together reveal a type of liquid particle localization we call 2D caged motion characterized by large nonergodicity parameter but shorter—not longer—caging times, unlike caged motion in glassy systems. In Sec. IV, we discuss how thermal

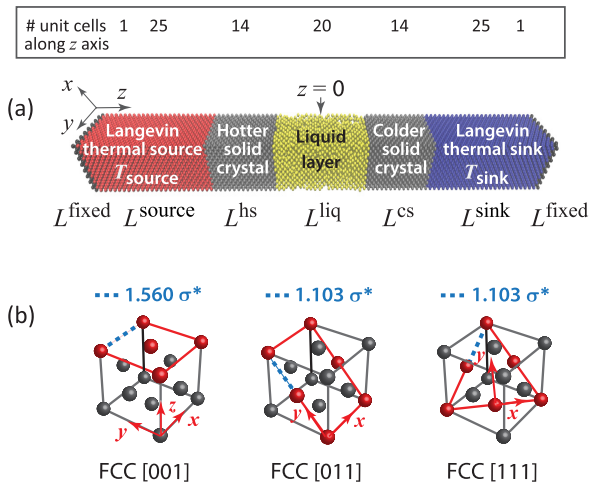

FIG. 2. (a) Multilayer rectangular cell with fixed exterior boundary temperature $T_{\rm source} = 1.6$ and $T_{\rm sink} = 1.0$. Shown is the number of FCC unit cells comprising each layer. (b) Three FCC facets used in this paper. Dimensions of the rectangular cell are listed in Table II. Coordinate values of the reciprocal lattice vectors are listed in Table III.

tunneling across the L/S interface for the [011] facet, which exhibits the smallest thermal slip length, arises from the anisotropy of the solid surface potential. In Sec. V, we summarize key findings.

II. COMPUTATIONAL DETAILS

The NEMD system in Fig. 2(a) consisted of a simple monatomic liquid confined between two crystals identically oriented along one of three facet planes of the FCC unit cell in Fig. 2(b). All relevant variables, scalings, and parameter values can be found in Table I. The thermal source and sink temperatures were maintained at the values $T_{\rm source} = 1.6$ and $T_{\rm sink} = 1.0$, as described in Sec. II A. Sublimation from the outermost thermostatted layers of the rectangular cell (i.e., region $L^{\rm fixed}$) was prevented by affixing those particles in place. Different values of the thermal flux J_z were generated naturally by choice of facet and L/S interaction energy, which ranged from the nonwetting ($\varepsilon_{\rm LS} = 0.1$) to wetting ($\varepsilon_{\rm LS} = 1.0$) regime. The density of the liquid layer was set by initially situating particles on the sites of the FCC lattice and then sequentially removing particles until the density of the liquid bulk interior equalled $\rho_{\rm bulk} \approx 0.84$. The central plane of the liquid layer was situated at the coordinate origin $z = 0$.

Particle pairs $(ij) =$ LL, LS, or SS in the solid and liquid layers were made to interact through a truncated and shifted Lennard-Jones potential, also called the Weeks-Chandler-Anderson potential, given by

$$U_{ij}(r) = \begin{cases} U(r) - U(r_{\rm c}) & \text{if } r \leqslant r_{\rm c} \\ 0 & \text{if } r > r_{\rm c}, \end{cases} \tag{4}$$

where

$$U(r) = 4\,\varepsilon_{ij}\left[\left(\frac{\sigma_{ij}}{r}\right)^{12} - \left(\frac{\sigma_{ij}}{r}\right)^{6}\right], \tag{5}$$

TABLE I. Symbols, numerical values, and scalings for nondimensionalization of physical quantities based on fluid argon [38–40]. Superscripts with an asterisk signify dimensional quantities. Boltzmann's constant $k_B = 1.380649 \times 10^{-23}$ J/°K.

Physical quantity	Numerical value
Mass	$m^* = 6.690 \times 10^{-26}$ kg
Length	$\sigma^* = 0.3405 \times 10^{-9}$ m
Energy	$\epsilon^* = 165.3 \times 10^{-23}$ J
Temperature	$T^* = \epsilon^*/k_B = 119.8$ °K
Time	$t^* = (m^*\sigma^{*2}/\epsilon^*)^{1/2} = 2.14$ ps
Mass density	$\rho^* = m^*/(\sigma^*)^3$
Pressure	$p^* = \epsilon^*/(\sigma^*)^3 = 0.4187$ MPa
Effective particle diameters	$\sigma^*_{\rm LL} = \sigma^*_{\rm LS} = \sigma^*_{\rm SS} = \sigma^*$
FCC edge length	$a^* = 1.560\,\sigma^* = 5.382 \times 10^{-10}$ m
Interaction energies	$\epsilon_{\rm LL} = \epsilon^*$
	$\epsilon_{\rm LS} = 0.1 - 1.0\,\epsilon^*$
	$\epsilon_{\rm SS} = 10\,\epsilon^*$
Variable	**Value in scaled units**
Solid or liquid particle mass	1
LJ repulsive distance	$\sigma_{\rm LL} = \sigma_{\rm LS} = \sigma_{\rm SS} = 1.0$
FCC edge length	$a = 1.560$
Integration time step	$\Delta t_{\rm int} = 0.002$
Source temperature	$T_{\rm source} = 1.6$
Sink temperature	$T_{\rm sink} = 1.0$
LJ interaction energy	$\varepsilon_{\rm LL} = 1$
	$\varepsilon_{\rm LS} = 0.1 - 1.0$
	$\varepsilon_{\rm SS} = 10$
Bulk liquid density	$\rho_{\rm L} \approx 0.84$
FCC unit cell density	$\rho_{\rm S} = 1.0536$

and $r = |\vec{r}|$ is the particle separation distance, ε_{ij} is the pairwise interaction energy, and σ_{ij} is the pairwise separation distance where $U(r = \sigma_{ij}) = 0$. The cutoff radius was set to $r_{\rm c} = 2.5$. In contrast to most NEMD studies, we used a shifted and truncated LJ potential to ensure no discontinuity in the force fields and therefore no spurious impulsive effects which might potentially influence the motion.

The construction of the solid layers is an important issue. Some NEMD studies rely on the so-called harmonic wall-spring model in which solid wall particles are tethered to frozen lattice sites by a Hookean force and allowed to vibrate about those positions [27,41]. Solid walls can instead be

TABLE II. Dimensions for the geometry in Fig. 2(a).

Cell dimensions (scaled by σ^*)	[001]	[011]	[111]
L_x	12.48	12.48	13.24
L_y	12.48	13.24	13.37
$L^{\rm fixed}$ (1 unit cell per end)	1.56	1.10	1.80
$L^{\rm source}$	39.00	39.71	40.53
$L^{\rm hs}$	21.84	22.06	21.17
$L^{\rm liq}$	31.20	30.89	29.72
$L^{\rm cs}$	21.84	22.06	21.17
$L^{\rm sink}$	39.00	39.71	40.53
Total length along z axis	156.00	156.64	156.72

TABLE III. Shortest 2D reciprocal lattice vectors (RLVs) for three Bravais planes (red) in Fig. 2(b): $\vec{k}_o = (2\pi/a^*)(\widehat{e}_x, \widehat{e}_y)$ for [001], $(2\pi/a^*)(\widehat{e}_x, 0)$ for [011], and $(2\pi/a^*)(\sqrt{2}\widehat{e}_x, \sqrt{2/3}\widehat{e}_y)$ and $(2\pi/a^*)(0, \sqrt{8/3}\widehat{e}_y)$ for [111]. Next shortest RLVs for [011] also shown.

FCC facet	$k_{o,x}$	$k_{o,y}$
[001]	±4.03	±4.03
[011] (shortest)	±4.03	0.00
[011] (next shortest)	0.00	± 5.70
[111]	±5.70	±3.29
	0.00	± 6.58

constructed using a strong-binding LJ potential, which has been shown to yield accurate values of mechanical and interfacial properties of FCC metals [12]. The solid layers in our study were also constructed in this way to ensure propagation of anharmonic modes as well. Since the melting temperature of an LJ solid is estimated to be $T_m \simeq 0.5 \times \varepsilon_{SS}$ [42], the choice for S/S interaction energy $\varepsilon_{SS} = 10$ ensured that the crystal remained in the solid state for the range of temperatures generated.

A. Temperature control

The NEMD simulations were conducted with the open source package LAMMPS [43,44]. Periodic boundary conditions were enforced along the $\hat{x}$ and $\hat{y}$ axes. The liquid and solid layers were first equilibrated with a Nosé–Hoover thermostat [45] with $T_{\text{equil}} = 1.3$ for a period $10^5 \Delta t_{\text{int}} = 200$ to enforce NVT conditions. This thermostat was then switched off and particles constituting the thermal source and sink layers [see Fig. 2(a)] were subject to the Langevin equation [46],

$$\frac{d^2\vec{r}_i}{dt^2} = -\sum_{i\neq j} \frac{dU_{ij}(r)}{dr}\hat{r}_i - \frac{1}{\tau_{\text{damp}}}\frac{d\vec{r}_i}{dt} + \vec{F}_{\text{stoch}}, \tag{6}$$

where $\vec{r}_i$ is the 3D coordinate of particle i, $\vec{F}_{\text{stoch}}$ is a random force vector given by a normal distribution of magnitude $[T_{\text{set}}/(\tau_{\text{damp}}\,\Delta t_{\text{int}})]^{1/2}$, and T_{set} is the set point temperature. The damping constant was chosen to be $\tau_{\text{damp}} = 500\ \Delta t_{\text{int}} = 1.0$. It was confirmed that for the range of induced temperatures, the interior of the fluid remained a well-defined dense liquid far from any critical or triple point [40,47]. After activation of the Langevin thermostats, the system was stabilized for an additional period $2 \times 10^5 \Delta t_{\text{int}} = 400$ to ensure steady-state conditions. The trajectories of particles in the unthermostatted layers were then obtained by integration of Newton's equations using the Verlet method [39] based on a time step $\Delta t_{\text{int}} = 0.002$.

The thermal flux J_z propagating across the unthermostatted layers was computed from

$$J_z = \frac{1}{L_x \times L_y}\frac{E_{\text{net}}(t)}{t}, \tag{7}$$

where $E_{\text{net}}(t)$ was the net thermal input during the time interval t required to maintain the Langevin thermostats at their set point temperature. The net input E_{net} was confirmed to be increased linearly in time as required for stationary behavior. Thermal conductivity values within the interior liquid and solid layers were estimated from the ratio $k = J_z/|dT/dz|$. (The values of k listed in the Appendix are only for reference and were not used in any analysis.)

The thickness of the thermostatted solid layers was selected to exceed the length of the estimated phonon mean-free path Λ to avoid inaccurate reduction in the value of TBR [48]. It has been shown that for $\Lambda = c_\ell \times \tau_{\text{damp}} \leqslant 2L$, where c_ℓ is the speed of longitudinal sound waves [22] and L the solid layer thickness, phonons are dissipated before undergoing reflection and propagation from the exterior boundary to the L/S interface. The speed c_ℓ within an FCC crystal can be approximated [42] from the relation $c_l = 9.53\sqrt{\varepsilon_{SS}}$. For the parameter values used in our study ($\varepsilon_{SS} = 10$, $\tau_{\text{damp}} = 1$ and $L^{\text{source}} = L^{\text{sink}} \approx 40$), the inequality $\Lambda = c_\ell \times \tau_{\text{damp}} = 9.53\sqrt{10} \simeq 30 \leqslant 2L \lesssim 81$ was well satisfied.

The virial contribution to the pressure in the interior of the liquid layer was also confirmed to depend only weakly on ε_{LS} or facet type. Specifically, the virial pressure at $\varepsilon_{LS} = 0.1$ was measured to be 2.72 ± 0.03 for [001], 2.78 ± 0.02 for [011], and 2.86 ± 0.02 for [111] and at $\varepsilon_{LS} = 1.0$ was 2.54 ± 0.02 for [001], 2.60 ± 0.03 for [011], and 2.66 ± 0.03 for [111]. Since the interior liquid temperature hovered about $T = 1.3$, the kinetic contribution to the pressure (roughly 1.5) did not vary. Relative to the influence of other effects, the bulk liquid pressure was not a contributing factor to the relative reduction in thermal slip length. We also note that the liquid pressures in our system were far below those required to reduce thermal boundary resistance in L/S systems in any significant way [22].

B. Averaging procedure for time-independent quantities

After confirmation of steady-state conditions, simulations were run for a total time $t_{\text{total}} = 5 \times 10^6 \Delta t_{\text{int}} = 10^4$ with data sampled at a rate $500\Delta t_{\text{int}} = 1.0$. The sampling rate was chosen to match the decay time of the velocity autocorrelation function (see Fig. 12). This data was then divided into ten equal nonoverlapping segments representing ten ensembles. The angular brackets $\langle \cdot \rangle$ in this paper signify the mean with standard deviation computed from the average over these ensembles.

The distribution of various physical quantities along the $\hat{z}$ axis was obtained by partitioning the liquid and solid layers into nonoverlapping bins of area $L_x \times L_y$ and width Δz_{bin}. To ensure sufficient resolution for discerning oscillations in liquid density near the L/S interface, the bin width was set to $\Delta z_{\text{bin}} = 0.016$ and the bin density ρ_{bin} estimated from $\langle N_{\text{bin}}\rangle/V_{\text{bin}}$ based on the average number of particles in the bin $\langle N_{\text{bin}}\rangle$. (The bin volumes for the measurements of density were therefore 2.49 for [001], 2.64 for [011], and 2.83 for [111]). The contact density ρ_c was obtained by integrating the liquid density profile over the distance separating adjacent minima in the first oscillation in $\rho(z)$ near the solid surface.

A coarser resolution $\Delta z_{\text{bin}} = 0.785$ was used for extracting the temperature distribution $\langle T(z)\rangle$. Too small a bin width caused excessively noisy velocity and thermal profiles arising from rapid fluctuations in N_{bin}. It was confirmed that even for the smaller bin width $\Delta z_{\text{bin}} = 0.016$, $\langle T(z)\rangle$ did not exhibit oscillations near the L/S interface. The average bin temperature T_{bin} was estimated from the equipartition

relation,

$$T_{\rm bin} = \left\langle \frac{1}{3N_{\rm bin}} \sum_{i}^{N_{\rm bin}} \vec{v}_i^{\,2} \right\rangle, \tag{8}$$

where $\vec{v}_i = (v_x, v_y, v_z)_i$ for particle i.

The thermal jump ΔT across the L/S boundary was measured to be the temperature difference midway between the peak solid and peak liquid density using the values extrapolated from the respective thermal gradient within the interior solid and liquid layers. The thermal slip length evaluated from Eq. (3) therefore differed between the hotter and colder sides of the liquid layer.

The planar configuration of particles in the contact layer, liquid interior, and first solid layer were evaluated from the static 2D radial distribution function given by

$$g^{\parallel}(r) = \left\langle \frac{L_x \times L_y}{N_{\parallel}} \frac{n_{\rm pairs}(r)}{2\pi r \Delta r} \right\rangle, \tag{9}$$

where $N_{\parallel}$ is the number of particles in the layer and $n_{\rm pairs}$ is the number of particle pairs within an annulus of radius $r - \Delta r/2 \leqslant r \leqslant r + \Delta r/2$ with $\Delta r = 0.01$. Here and throughout this paper, the superscript $\parallel$ refers to measurements extracted from solid or liquid layers which lie parallel to the L/S interface. The long-range order within that layer was extracted from the 2D static structure factor [49]

$$S_c^{\parallel}(\vec{k}) = \left\langle \frac{1}{N_c^2} \sum_{p=1}^{N_c} \exp(i\vec{k}\cdot\vec{r}_p) \sum_{q=1}^{N_c} \exp(-i\vec{k}\cdot\vec{r}_q) \right\rangle, \tag{10}$$

normalized such that $0 \leqslant S_c^{\parallel}(\vec{k}) \leqslant 1$, where $\vec{k} = (k_x, k_y)$ and N_c is the number of particles in the contact (c) layer. It was confirmed that contributions from the imaginary part of Eq. (10) were negligible.

C. Averaging procedure for time-dependent quantities

Analysis of the dynamical motion in the contact layer was restricted to those trajectories of ten or more particles which remained within the layer, never having escaped. Particles which escaped and then returned to the layer were excluded from this analysis. Averages of dynamical quantities were carried out using an ensemble averaging scheme based on three time blocks, which nonetheless led to acceptably small standard deviations. Within each time block, measurements were initiated at different times $t_o = (0, 10, 20, \ldots, 475, 000) \times \Delta t_{\rm int}$ and data subsequently sampled at small intervals $10\Delta t_{\rm int} = 0.02$. Data collection spanned the period $t_o \leqslant t \leqslant t_o + t_f$, where t_f denotes the time at which only ten or more particles from the original set of occupants at t_o remained. In all cases, t_f exceeded the decay time of the velocity autocorrelation (Fig. 12) function by at least an order of magnitude. Since each start time t_o yielded different values of t_f, the shortest time t_f within a block was used to estimate averages for that block and the shortest time t_f of the three blocks then used to compute the average reported. Later, we shall refer to this block averaged time as the retention time t^* associated with 2D caged dynamics. In what follows, quantities indicated by the symbol $\langle\cdot\rangle_{t_o}^{B}$ signify the ensemble average based on averages over start times t_o followed by three-block averaging.

Dynamical motion of particles in the contact layer exhibited different regimes, as quantified in two ways. The 2D mean-squared displacement was evaluated from the relation

$$\mathrm{MSD}_c^{\parallel}(t) = \left\langle \frac{1}{N_c} \sum_{j}^{N_c} |\vec{r}_j(t_o + t) - \vec{r}_j(t_o)|^2 \right\rangle_{t_o}^{B}, \tag{11}$$

where the 2D velocity for particle j is $\vec{r}_j(t) = [x_j(t), y_j(t)]$. Here, $N_c = N_c(t_o, t_f)$ is the number of particles which remained in the contact layer throughout the entire interval $t_o \leqslant t \leqslant t_o + t_f$ subject to the constraint $N_c \geqslant 10$. The 2D self-intermediate scattering function was evaluated according to

$$F_c^{\parallel}(\vec{k}_o, t) = \left\langle \frac{1}{N_c} \sum_{j=1}^{N_c} \exp\{i\vec{k}_o \cdot [\vec{r}_j(t_o + t) - \vec{r}_j(t_o)]\} \right\rangle_{t_o}^{B}, \tag{12}$$

where $\vec{k}_o$ is the wave vector corresponding to the maximum peak in the structure factor. (The wave vector $\vec{k}_o$ did not always coincide with the smallest reciprocal lattice vector (RLV) of the adjacent solid facet, as discussed in Sec. III.) It was confirmed that contributions from the imaginary part of Eq. (12) were negligible. Both the 2D and 3D velocity autocorrelation function

$$\mathrm{VACF}_c^{\parallel}(t) = \left\langle \frac{1}{N_c} \sum_{j=1}^{N_c} \vec{v}_j(t_o + t) \cdot \vec{v}_j(t_o) \right\rangle_{t_o}^{B} \tag{13}$$

were computed for quantifying particle motion within the contact layer.

III. RESULTS

Here we present results of various measurements quantifying the structure and dynamics of motion in the contact layer. Measurements of all quantities described can be found in the Appendix.

A. Local equilibrium of contact layer

Listed in Table IV is the average number of particles within the hotter and colder contact layers for different facets and $\varepsilon_{\rm LS} = 0.1$ or 1.0. For a given facet, there are always more particles in the colder layer, ranging from about 5.5% more than the hotter layer for the nonwetting [001] facet to more than 20% for the wetting [111] facet. For the [001] and [111] case, increasing the L/S bonding strength from 0.1 to 1.0 increases the occupation number. By contrast, the more wetting layer against the [011] facet incurs a substantial decrease in occupation number of about 25%–30% depending on the layer temperature. In Sec. III B 5, we discuss an interesting structural transition which occurs in the contact layer against the [011] facet which is responsible for this decrease.

The data in Fig. 3 represent the typical spread in the speed of particles within the contact layer, as represented by the Maxwell-Boltzmann distribution (in reduced units),

$$\mathcal{P}(v_i) = 4\pi \left(\frac{1}{2\pi T}\right)^{3/2} v_i^2 \exp\left(-\frac{v_i^2}{2T}\right) \quad \text{for } i \in N_c, \tag{14}$$

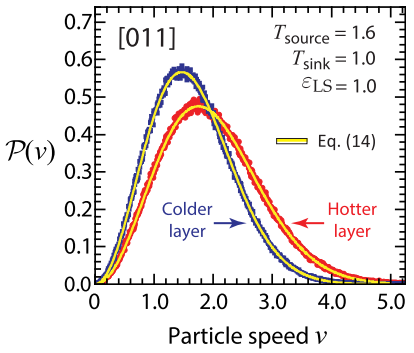

FIG. 3. Maxwell-Boltzmann distribution of particle speeds in the hotter and colder contact layer for the [011] facet and $\varepsilon_{LS} = 1.0$. Least-squares coefficients: $T_c^{\text{hotter}} = 1.526 \pm 0.001$ and $T_c^{\text{colder}} = 1.0740 \pm 0.0009$ for Eq. (14) and $T_c^{\text{hotter}} = 1.529 \pm 0.006$ and $T_c^{\text{colder}} = 1.074 \pm 0.004$ for Eq. (8).

where N_c is the total number of particles i in the contact layer and $v_i^2 = (v_{i,x})^2 + (v_{i,y})^2 + (v_{i,z})^2$. The agreement confirms that the contact layer maintains a state of local thermal equilibrium, which therefore validates estimates of the layer temperature obtained from the equipartition relation in Eq. (8).

B. Time-independent metrics of contact layer

The following subsections describe results of measured stationary properties used to elucidate the thermal response and spatial configuration of particles within the contact layer.

1. *Influence of crystal facet, L/S interaction energy, and temperature on contact layer density*

Molecular dynamics studies of systems in thermal equilibrium [30–32,50,51] and nonequilibrium [15,16,22,52–55] have demonstrated that a fluid in contact with a featureless or structured solid wall exhibits an oscillatory density profile $\rho(z)$ which rapidly decays toward the bulk interior value. The distance between oscillations scales closely with the effective particle diameter σ specified by the LJ potential. The number and amplitude of oscillations increases as temperature decreases or ε_{LS} increases, evident from Figs. 4(a)–4(f).

The results in Figs. 4(a)–4(f) confirm that the spacing of crystal planes is smallest for the [011] and largest for the [111] facet. Also, the peak solid density is largest for [111] and smallest for [011]. Both features are expected from the facet planes shown in Fig. 2(b). The degree of liquid layering indicated by the number, amplitude, and width of the oscillations is smallest for the [011] and largest for the [111] facet. This reduced stratification indicates that particles in the contact layer against the [011] facet experience higher mobility along the $\hat{z}$ axis and slowest mobility against the [111] facet. At the hotter and colder L/S interface, it is also apparent that the particles against the [011] facet undergo a structural transition at a certain value of ε_{LS} which depends on local temperature. This transition, particularly noticeable at the hotter interface, can be seen from the abrupt shift in the location of the first oscillation. For values ε_{LS} above this transition, the depletion layer thickness for the [011] case

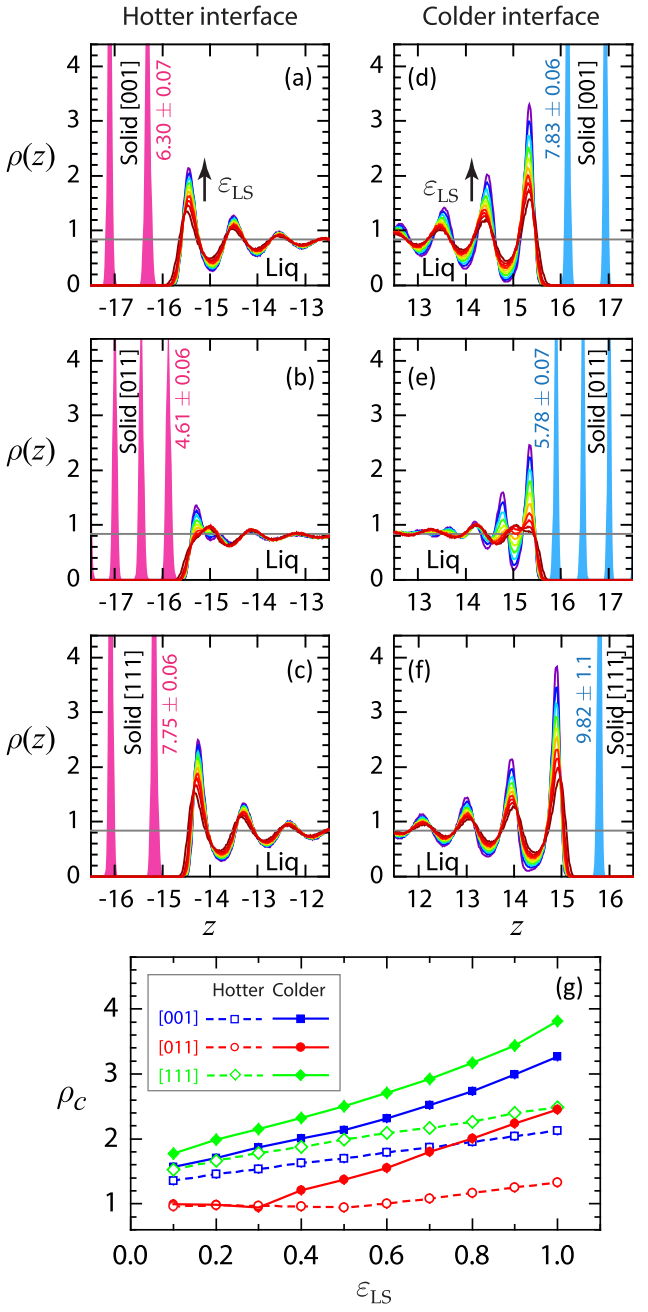

FIG. 4. (a)–(f) Liquid density $\rho(z)$ at the hotter and colder L/S interface for three facets and $0.1 \leqslant \varepsilon_{LS} \leqslant 1.0$ in increments of 0.1. Shown also are the first few peaks representing the density of the crystal planes for $\varepsilon_{LS} = 1.0$ (full magnitude not shown). Solid horizontal line (grey) denotes bulk liquid value $\rho_{\text{bulk}} = 0.84$. Numerical values listed next to the first solid layer indicate the peak value in the solid density distribution (extracted with bin width $\Delta z = 0.016$). (g) Contact density ρ_c at the hotter and colder L/S interface versus ε_{LS} for different crystal facets. (Error bars are smaller than the icon size).

decreases while that for the [001] and [111] undergo a slight increase. That said, the depletion layer thickness for the liquid facing a [011] facet is always the smallest of all three facets no matter the value ε_{LS}.

Shown in Fig. 4(g) are the values of the contact density ρ_c at the hotter and colder L/S interface for increasing

value $\varepsilon_{\rm LS}$ and three facet planes. In all cases, ρ_c rises monotonically with increasing $\varepsilon_{\rm LS}$, although the slope of the rise is highest for colder temperatures. For fixed value $\varepsilon_{\rm LS}$, ρ_c is always smallest for the [011] case by a significant amount and largest for the [111] case. The structural transition noted above for the [011] case seems evident here too but only for the colder layer. Above the transition near $0.3 \lesssim \varepsilon_{\rm LS} \lesssim 0.4$ for the [011] case, ρ_c shows increasing deviation between the hotter and colder layers with increasing $\varepsilon_{\rm LS}$. It is well-known that the interfacial energy density (i.e., energy per unit area of the interface) of liquid particles adjacent to a solid surface is comprised of three distinct contributions, namely, the Gibbs surface excess energy, the excess entropy, and the excess number of absorbed liquid particles [50]. Future studies of these relative contributions for increasing value $\varepsilon_{\rm LS}$, different facets and different local temperatures can yield additional insight into the mechanism driving the structural transition of the contact layer against the [011] facet.

2. Influence of crystal facet and L/S interaction energy on thermal distribution and thermal flux

Shown in Figs. 5(a)–5(c) are the temperature profiles $T(z)$ in the solid and liquid layers. The sizable jumps at the hotter and colder L/S interface confirm the effects of thermal boundary resistance. Away from the interface, the profiles are strongly linear and the thermal gradient therefore constant, confirming that the solid and liquid layers represent Fourier materials. The liquid density is not symmetric about the central axis $z = 0$ and should not be since it varies with temperature and pressure. At steady-state conditions, energy conservation requires that for fixed value $\varepsilon_{\rm LS}$ and given facet, the thermal flux J_z must be a constant independent of position z. Since liquids have a smaller thermal conductivity than solids, the liquid layer exhibits a larger thermal gradient whose magnitude increases with $\varepsilon_{\rm LS}$, thereby producing a smaller thermal jump.

Measured values of the thermal flux, thermal gradient, and thermal conductivity can be found in Table V—values of the thermal jump and contact layer temperature can be found in Table VI. Those data reveal that for a given value $\varepsilon_{\rm LS}$, the thermal jump ΔT is not necessarily always larger on the colder side, as one might naively intuit. The measurements in Table VI confirm that for the same value $\varepsilon_{\rm LS}$, the ratio $\Delta T|_{\rm hotter}/\Delta T|_{\rm colder}$ can be smaller, equal to, or even larger than one. This is due to the fact that the thermal flux J_z depends not only on $\varepsilon_{\rm LS}$ and facet plane but also local temperature. It is for this reason that a proper comparison between systems using either TBR or the slip length L_T must incorporate normalization by the thermal flux, as given by Eqs. (1) and (3). Shown in Fig. 5(d) is the monotonic increase in J_z with increasing $\varepsilon_{\rm LS}$. For fixed value $\varepsilon_{\rm LS}$, the flux across the [011] facet is always highest. Inspection of the results in Figs. 4(a)–4(f) indicate that the interface with the smallest depletion layer, namely, the [011] facet, sustains the highest thermal flux. Such a correlation has been observed in other systems involving water on silicon and water on graphene-coated silicon [37].

3. Influence of crystal facet, L/S interaction energy, and temperature on thermal slip length

Shown in Fig. 6(a) is the thermal slip length extracted from the hotter and colder L/S interface with increasing $\varepsilon_{\rm LS}$. For all cases, L_T decreases monotonically with increasing $\varepsilon_{\rm LS}$. The decay is more rapid for $\varepsilon_{\rm LS} \lesssim 0.6$ and more gradual above that value, indicating less sensitivity to $\varepsilon_{\rm LS}$ for more wetting liquids. At a fixed value $\varepsilon_{\rm LS}$, L_T is always smallest for the [011] facet by a noticeable amount and largest for the [111] facet. A reduction in L_T with increasing $\varepsilon_{\rm LS}$ has been reported in many NEMD studies [17,18,55] utilizing different types of thermostats, different liquids and solids, and different thermal conditions, but no general relation has been proposed. The solid and dashed lines in Fig. 6(a) represent least-squares fits to the quadratic relation

$$L_T(\varepsilon_{\rm LS}) = a - b\,\varepsilon_{\rm LS} + c\,\varepsilon_{\rm LS}^2, \tag{15}$$

where a, b, and c are positive constants, which depend on facet plane and contact layer temperature T_c. The fit coefficients are listed in Table VII.

Shown in Fig. 6(b) are the values L_T versus the contact layer density ρ_c. Here, of course, the variable ρ_c is not an input parameter but a measured quantity. Except for a few notable points, the thermal slip length generally decreases monotonically with increasing value ρ_c, reflecting the influence of the L/S interaction energy. At both the hotter and colder L/S interfaces, it is clear that L_T achieves the smallest value for the [011] facet and the largest value for the [111] facet. The solid and dashed lines represent least-squares fits to the reciprocal function

$$L_T(\rho_c) = \frac{\alpha_1}{\rho_c - \alpha_2}, \tag{16}$$

where α_1 and α_2 are positive constants which depend on facet plane and T_c. The fit coefficients can be found in Table VIII. For the [011] case, the data points on the colder side for $\varepsilon_{\rm LS} = 0.1, 0.2, 0.3$ and on the hotter side for $0.1 \leqslant \varepsilon_{\rm LS} \leqslant 0.7$ show larger deviations from Eq. (16). These points represent those systems whose values $\varepsilon_{\rm LS}$ fall below the structural transition value noted earlier.

Taken together, the results in Figs. 4(g), 5(d), and 6(b) are seemingly counterintuitive. For fixed value $\varepsilon_{\rm LS}$, a hotter or colder contact layer against the [011] facet facilitates the largest thermal flux J_z among the three facets despite featuring the smallest—not largest—contact density ρ_c. This demonstrates that a larger contact density is not a unique predictor of higher thermal flux (nor smaller thermal resistance nor higher thermal conductance) as often suggested [22,35,36]. In the original acoustic mismatch model proposed by Khalatnikov [56,57], the analytic relation for thermal boundary resistance was shown to depend on several variables including local temperature, liquid pressure, elastic properties of the bulk liquid and solid, excitation spectra of electrons, and different phonon branches of the solid. In classical or quantum systems changes in one or more variables can be potentially offset by others such that no one variable is a unique predictor of $\mathcal{R}$ or L_T.

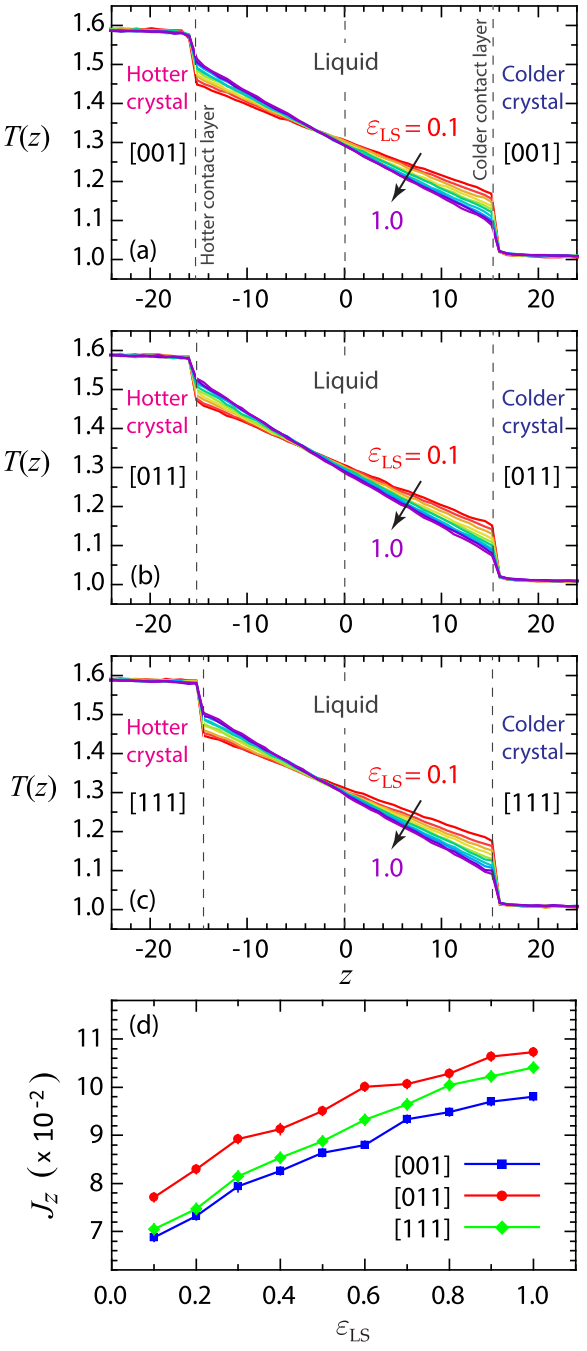

FIG. 5. (a)–(c) Steady-state temperature distribution $T(z)$ throughout the solid and liquid layers for three facet planes and $0.1 \leqslant \varepsilon_{LS} \leqslant 1.0$ in increments of 0.1. (d) Corresponding values of the steady thermal flux J_z. Connecting segments are only a guide to the eye.

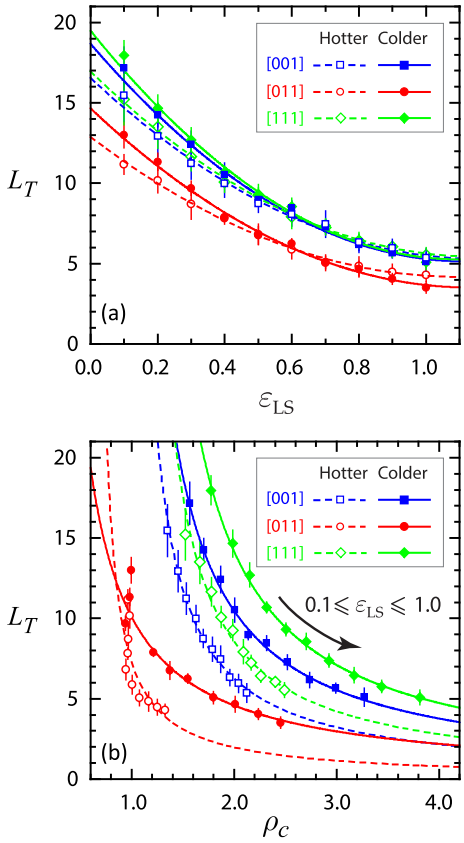

FIG. 6. Reduction in the thermal slip length L_T with (a) increasing L/S interaction energy ε_{LS} and (b) increasing contact density ρ_c at the hotter and colder interface for three facet planes. Superposed solid and dashed curves represent least-squares fits to Eqs. (15) and (16), with fit constants listed in Tables VII and VIII, respectively.

4. Influence of crystal facet, L/S interaction energy and temperature on 2D radial distribution function of contact layer, and first crystal plane

Shown in Fig. 7 are the 2D radial distribution functions $g^{\parallel}(r)$ for contact layer particles at the hotter and colder L/S interfaces for three facet planes and increasing value ε_{LS} (colored curves). Superposed are the results for the liquid interior as well (black curve). The shaded peaks are the results for the first crystal plane for $\varepsilon_{LS} = 1.0$. It was confirmed that $g^{\parallel}(r)$ within the liquid interior is relatively insensitive to ε_{LS}, as expected given $10 \lesssim \varepsilon_{SS}/\varepsilon_{LS} \lesssim 100$.

In general, the results show that colder temperature and stronger L/S coupling enhances commensurability in the radial configuration of particles between the contact layer and crystal facet. For the [011] case at smaller values ε_{LS}, both the position and shape of the first two liquid peaks closely resemble those of the liquid interior, with a small but gradual mismatch as r increases. As evident, the local distribution of particles in the contact layer is much more isotropic and therefore more liquidlike than liquid particles against the [001] or [111] facet. This is quite obvious for the colder layer for $\varepsilon_{LS} \lesssim 0.3$ and the hotter layer for $\varepsilon_{LS} \lesssim 0.7$. These happen to be the same cases noted earlier, which exhibit deviations from the reciprocal curves in Fig. 6(b). The results in Fig. 7 also demonstrate that while the contact layer against the [001] or [111] facet undergoes a smooth and gradual increase in $g^{\parallel}(r)$ with increasing ε_{LS}, the layer against the [011] facet undergoes an abrupt jump signifying the structural transition noted earlier.

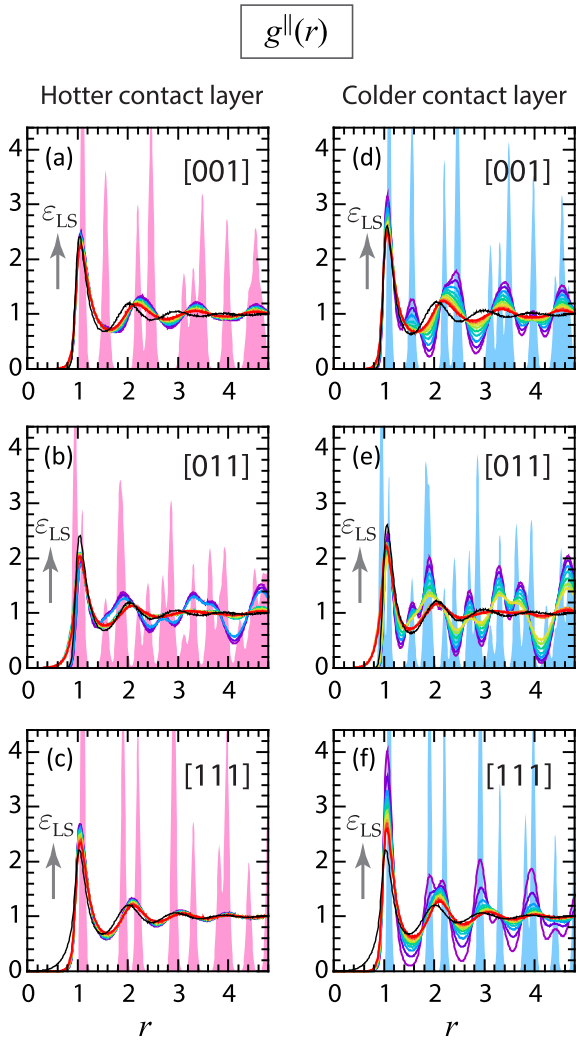

FIG. 7. (a)–(f) 2D radial distribution function $g^{\parallel}(r)$ given by Eq. (9) for the hotter and colder contact layer (colored curves) against three facets for $0.1 \leqslant \varepsilon_{LS} \leqslant 1.0$ in increments of 0.1. Shown also is $g^{\parallel}(r)$ for the interior liquid (black curve) and the first crystal plane for $\varepsilon_{LS} = 1.0$ (pink and blue shaded peaks).

5. *Influence of crystal facet, L/S interaction energy and temperature on 2D structure factor of the contact layer*

The results for the static 2D structure factor in Fig. 8 provide additional insight regarding commensurability and long range order between particles in the contact layer and crystal plane. The logarithmic scale in Fig. 8 spans three orders of magnitude. In general, at fixed value ε_{LS}, the colder the temperature, the more the structure factor of particles in the contact layer resembles that of the nearby crystal facet, as indicated by the set of discrete points (small red dots) signifying peak values of $S_c^{\parallel}(k_x, k_y)$. By contrast, the hotter the temperature, the more fluidlike the contact layer, as reflected by the formation of circular ring patterns. Irrespective of facet plane, the hotter contact layers for $\varepsilon_{LS} = 1.0$ show higher commensurability with the crystal surface than the colder contact layers for $\varepsilon_{LS} = 0.1$. Most notably, whether for $\varepsilon_{LS} = 0.1$ or 1.0, the [011] facet induces the strongest long range translational order.

Closer inspection of the images in Fig. 8 and other images for different values of ε_{LS} (not shown) revealed the definitive signature of the structural transition described earlier. Specifically, the global maxima of $S_c^{\parallel}(k_x, k_y)$ for the [001] or [111] case always coincide with the smallest RLVs of a given facet. For the [011] facet, that was the case only for values ε_{LS} above the structural transition noted earlier. Below that value, the global maxima coincide instead with the second smallest RLVs. This is evident when comparing the set of RLVs listed in Table III against those representing the maxima in Fig. 8. Therefore, while particles in the colder contact layer for $\varepsilon_{LS} \lesssim 0.3$ align preferentially along the $\hat{x}$ axis, those for $\varepsilon_{LS} \gtrsim 0.4$ instead align preferentially along the $\hat{y}$ axis. In hotter layers, this same switch in RLVs occurred near $0.7 \lesssim \varepsilon_{LS} \lesssim 0.8$.

The values corresponding to the structure factor maxima S_{max} versus ε_{LS} for the hotter and colder contact layers against three facet planes are shown in Fig. 9. While the results for the [001] and [111] facets reveal a smooth gradual increase with ε_{LS}, the [011] case manifests sizable jumps near $0.7 \lesssim \varepsilon_{LS} \lesssim 0.8$ for the hotter layer and $0.3 \lesssim \varepsilon_{LS} \lesssim 0.4$ for the colder layer, reflecting the structural transition noted. Above the transition, the magnitude of S_{max} significantly exceeds that of the other two facets. Below the transition, S_{max} for the colder layer against the [001] facet slightly exceeds that of the [011] facet, but this difference altogether disappears at higher temperature.

C. Time-dependent metrics of contact layer

The following subsections describe results of various dynamic properties used to elucidate the spatiotemporal behavior of particles exclusively confined to the contact layer throughout the measurement period.

1. *Influence of crystal facet, L/S interaction energy, and temperature on 2D mean-squared displacement within the contact layer*

Shown in Fig. 10 are a few sample snapshots from individual runs (i.e., not ensemble averaged) showing the location of particles in the hotter and colder contact layers for two values of ε_{LS} and three facet planes. The time t_{exit} denotes the instant at which one of four randomly tagged particles escaped the contact layer. As known, accurate inferences about particle dynamics requires extensive ensemble averaging, as described in Sec. II. However, instantaneous snapshots can nonetheless often reveal some interesting trends, as is the case here. The images shown indicate that for fixed facet and L/S bonding strength, a colder layer supports a higher particle density, longer exit time, and stronger commensurability between the configuration of liquid particles and the symmetry of the crystal surface potential. Inspection of the row of images for the [011] facet highlights a distinguishing feature in that an increase in L/S bonding strength causes a decrease in the number density, as noted earlier in Sec. III A and Table IV. For this particular facet, we also note that particles undergo hardly any displacement from their initial position for $\varepsilon_{LS} = 1.0$, suggestive of very strong localization induced by the crystal surface potential, and yet the exit times are the shortest not longest.

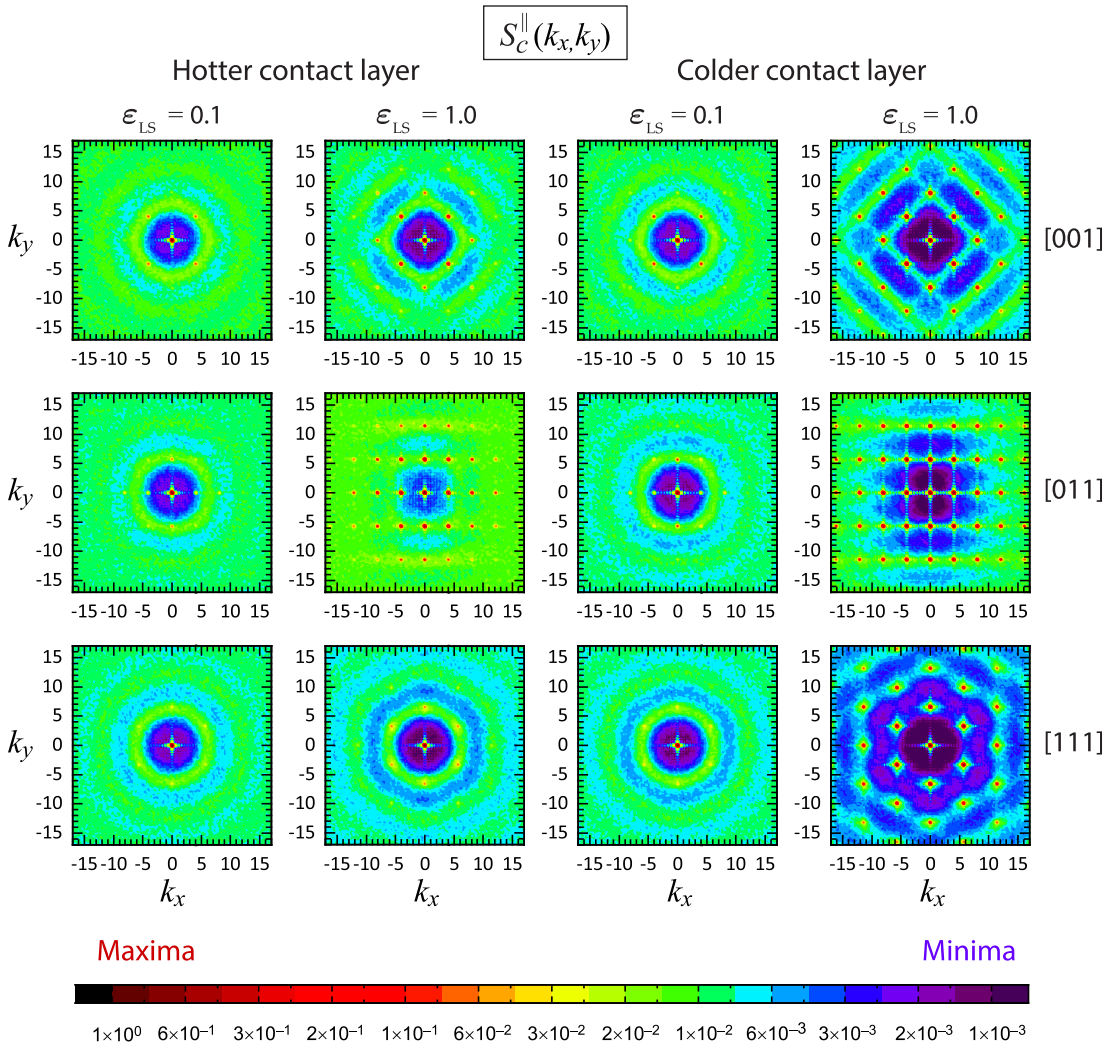

FIG. 8. Static 2D structure factor $S_c^{\parallel}(k_x, k_y)$ [Eq. 10] for the hotter and colder contact layers for two values of L/S interaction energy and three facet planes. Maximal values appear as small red dots.

The results in Fig. 11 represent measurements of the 2D mean square displacement $\mathrm{MSD}_c^{\parallel}(t)$ plotted on logarithmic axes for particles in the hotter and colder contact layers for three facet planes and $0.1 \leqslant \varepsilon_{\mathrm{LS}} \leqslant 1.0$. As noted in Sec. II C, different parameter values generated different average retention times and so the data end at different times. The solid lines in Figs. 11(a)–11(f) signify the theoretical exponents typical of the early (E) ballistic regime ($\gamma_E = 2$) and late (L) time diffusive regime ($\gamma_L = 1$) for ideal behaviors in a simple homogeneous and isotropic bulk fluid. As evident in Fig. 11(g), the influence of the solid surface potential diminishes the magnitude of both exponents. The early and late time exponents in Table IX were extracted from least-squares fits over early times $0.02 \leqslant t \leqslant 0.10$ and late times spanning the last full decade. For the plateaulike regime, least-squares fits were extracted from the last half-decade to compare exponents using the same time interval. Overall, the results show that 2D mean-square displacement against the [011] facet exhibits the largest deviation from $\gamma_L = 1$, underscoring the retarding influence of the crystal surface potential.

The six panels in Figs. 11(a)–11(f) reveal some additional features. Particles against the [001] and [111] facet undergo a smooth transition from the sub-ballistic to subdiffusive regime, with a small reduction in slope with increasing $\varepsilon_{\mathrm{LS}}$. By contrast, after the sub-ballistic regime, particles against the [011] facet either undergo subdiffusive motion or some type of 2D trapping or localization we shall coin as 2D caged motion. The different behavior is evident in Figs. 11(b) and 11(d), where there is a clear sizable gap in the data at a certain value $\varepsilon_{\mathrm{LS}}$ that depends on the local temperature. As suspected, this change in behavior coincides precisely with the structural transition described in Sec. III B 5. For late times, even for the smallest values $\varepsilon_{\mathrm{LS}}$, the [011] case still exhibits a noticeable departure from $\gamma_L = 1.0$, suggesting 2D caged motion in those systems as well, albeit much weaker.

The fitted exponents to the data in Figs. 11(a)–11(f) are plotted in Fig. 11(g) and tabulated in Table IX. The exponents γ_E, all below the ideal value 2, undergo a systematic small decrease with increasing $\varepsilon_{\mathrm{LS}}$, confirming that the short-range motion at early times is rather insensitive to facet plane and layer temperature and only weakly dependent on L/S

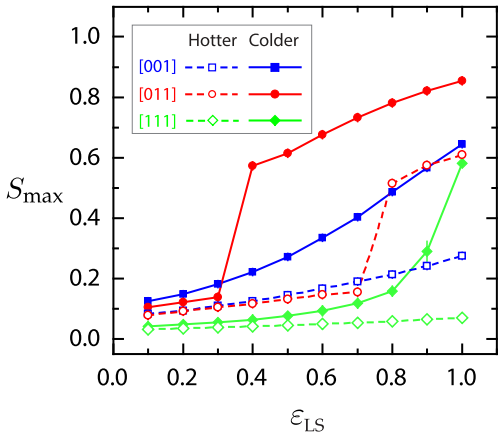

FIG. 9. Maxima of the static 2D structure factor S_{max} extracted from Eq. (10) for particles in the hotter and colder contact layers for three facets and $0.1 \leqslant \varepsilon_{LS} \leqslant 1.0$ in increments of 0.1. Connecting segments are only a guide to the eye.

interaction energy. This is expected given that ballisticlike motion is typically inertia dominated [58]. As for the temperature dependence of motion in the ballistic regime, it is known that $\mathrm{MSD}_c^{\parallel}(t) \sim T \times t^2$ [i.e., $(k_B T/m)t^2$ in dimensional units] for a simple homogenous and isotropic bulk fluid. Inclusion of hydrodynamic memory effects [59,60] augments the particle mass m by a slightly larger effective mass to account for the fraction of surrounding fluid displaced by the motion of the particle. The entries in Table IX along with the corresponding values of the contact layer temperature in Table VI confirm that hotter particles in the contact layer undergo larger mean-square displacement despite strong influence from the crystal surface potential.

The exponents γ_L, which all fall significantly below 1, span a much wider range. The [011] case, in particular, shows a strong dependence on local temperature and L/S interaction energy, unlike the other two facets. Particles against the [011] solid surface undergo the smallest displacements with a considerable slowdown after the structural transition noted earlier. Along with the results in Fig. 9, it is clear that the stronger the long-range order within a contact layer, induced by colder temperature or larger ε_{LS}, the greater the hindrance to planar diffusive displacement. As will be shown in Sec. IV, this hindrance is caused by significant repulsive energy barriers established by the crystal surface potential.

Inspection of the trends revealed by the retention times t^* based on the residency constraint applied reveals another important feature. In general, t^* increases with increasing ε_{LS} since particles take longer to escape the layer when experiencing stronger attraction to the solid surface. For the [011] case with ε_{LS} below the structural transition, the retention times are only slightly longer than those of the other facets. However, for values ε_{LS} above the transition, the [011] case yields significantly shorter retention times. In contrasting the behavior of the three facets at colder temperatures for the same value ε_{LS}, it is evident that the values t^* for [011] are almost an order of magnitude *smaller* and not larger, as is the case with caged motion in glassy systems. Therefore, while the in-plane motion of particles across the [011] facet is strongly suppressed due to 2D caging, particles are able to escape more rapidly into the third dimension (i.e., $\hat{z}$ axis). This trapping and release suggests a possible mechanism for the larger thermal flux in Fig. 5.

Under steady-state conditions, the average density of particles in a plane $\hat{x} - \hat{y}$ is a constant which depends only on the local temperature and pressure. On average then, for every particle that escapes the hotter contact layer, another cooler particle replaces it and soon thermally equilibrates to its new environment as the process repeats. On average, the 2D caged motion helps better funnel hotter particles to the adjacent cooler liquid layer more rapidly and efficiently by suppressing diffusive motion within the contact layer. At the colder L/S interface, caged motion helps funnel colder less energetic particles toward the adjacent warmer liquid layer and the vacancies get filled with warmer more energetic particles, thus propagating the thermal flux. While consideration of thermal energy alone explains the transport of heat from hotter to colder layers, the additional geometric restriction enforced by 2D caged motion provides more efficient particle tunneling, which leads to enhancement in the net thermal flux from warmer to cooler regions.

The 2D caged motion described is unlike 3D caged motion typically observed in equilibrium simulations of glass-forming liquids. 3D caged motion was originally observed in simple hard sphere models above the critical packing fraction [61] and in binary mixtures of LJ particles beyond the vitrification temperature [62]. It has since been studied in simulations of water, molten silicon, polymers, and long chain biological molecules as well. Glassy behavior caused by structural trapping from 3D caged motion commonly arises in systems with orientation-dependent intermolecular potentials. In such systems, the formation of a plateaulike region in the 3D mean-square displacement has been traced to two effects. Not only are individual particles trapped in cages formed by neighboring particles, but those neighbors are also situated within other cages, which causes an overall slowdown of the collective system [63]. The colder the temperature and the stronger the interparticle attraction, the stronger the caging effect and the longer the confinement time before re-escape and retrapping by another cage. The 2D caged motion we have described is rather different. While colder temperatures and stronger L/S bonding strengths cause stronger 2D caging, the confinement times become increasingly shorter as particles in the contact layer escape more readily in the $\hat{z}$ direction toward the adjacent liquid layer due to funneling facilitated by increasingly restricted motion within the $\hat{x} - \hat{y}$ plane.

2. Influence of crystal facet, L/S interaction energy, and temperature on 2D and 3D velocity autocorrelation within the contact layer

Caged motion can also be inferred from the velocity autocorrelation function. Early simulations of fluids in equilibrium modeled by LJ particles interacting via a soft repulsive potential $U(r) = \varepsilon_{LL}(\sigma/r)^{15}$ have shown that upon approach to vitrification, there develops a period of negative autocorrelation immediately following the ballistic regime [64,65]. This behavior has been attributed to the reversed motion of a particle undergoing collisions with neighboring particles which encircle it by a temporary mobile cage; the

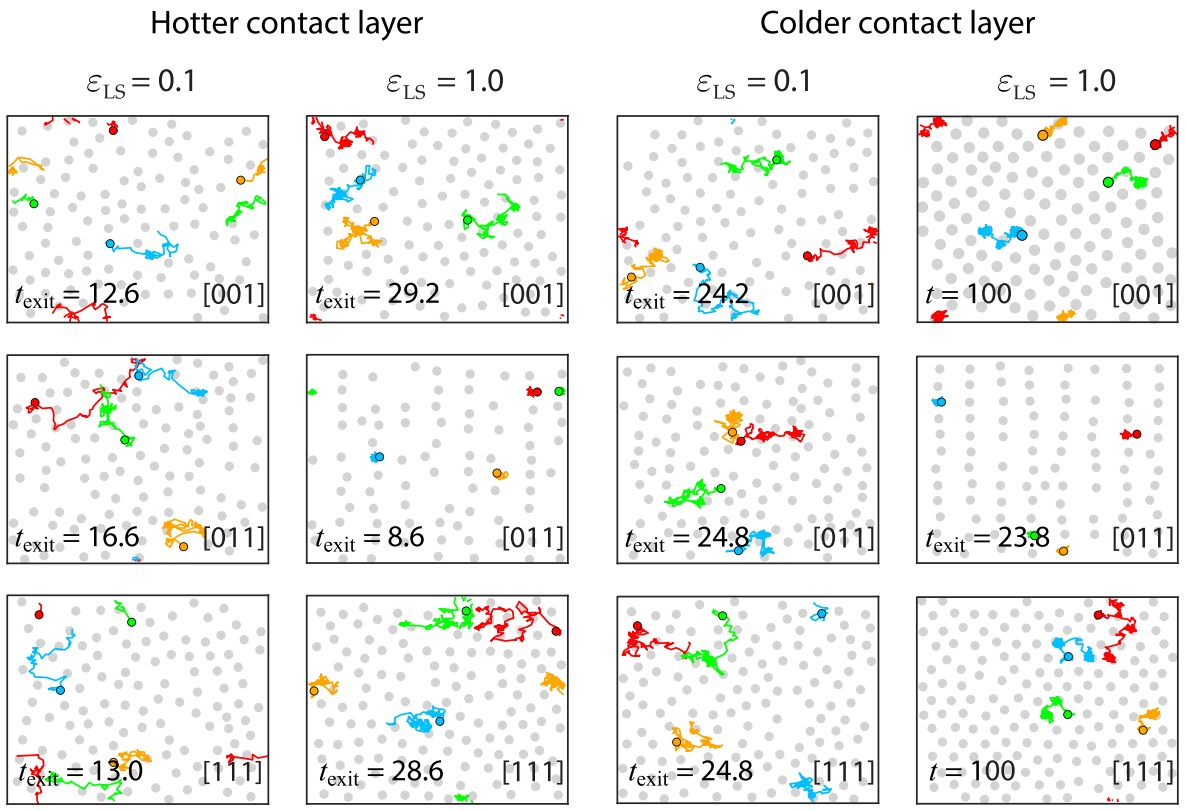

FIG. 10. Sample snapshots from individual runs (i.e., not ensemble averaged) showing the position of particles in the contact layer at t_{exit} (grey dots). Trajectories of four randomly tagged particles (red, green, yellow, and blue segments); final positions at t_{exit} are indicated by a black circle. Images marked $t = 100$ signify that tagged particles remained in the layer at least through that time.

inclusion of attractive forces enhances the cohesiveness or strength of the cage thereby prolonging the period of transient confinement.

Such negative autocorrelation is also demonstrated in Fig. 12, showing the results for the 2D and 3D velocity autocorrelation function evaluated from Eq. (13) for different facets, layer temperature, and two values of ε_{LS}. The autocorrelation essentially vanishes for $t \gtrsim 1.0$. Comparing the behaviors in Figs. 12(a) and 12(b) to the 2D mean-square displacement in Fig. 11 over the same time interval confirms that the start of negative autocorrelation coincides with the changeover from sub-ballistic to 2D caged motion. The magnitude of $\mathrm{VACF}_c^{\parallel}(t) < 0$ is always larger for colder layer temperature and larger value of ε_{LS} suggesting that smaller kinetic energy and strong L/S bonding correlates with stronger caging. The [011] system with $\varepsilon_{LS} = 1.0$ is the only case which exhibits a positive final oscillation prior to decay, which is likely related to stronger memory effects associated with stronger influence from the periodic crystal surface potential. An important distinguishing feature of motion against the [011] facet is also evident. For fixed value ε_{LS} and similar layer temperature, the [011] facet induces the *strongest* caging effect yet the interval of transient caging is *shortest*.

Comparison of the results for $\mathrm{VACF}_c^{\parallel}(t)$ with $\mathrm{VACF}_c^{3D}(t)$ indicates another distinction worth noting, which is perhaps more easily evident in the panels for $\varepsilon_{LS} = 1.0$. Irrespective of layer temperature and facet, the main contribution to the negative autocorrelation stems from 2D motion within the contact layer. This suggests that the dynamics of transient caging is due to repeated trapping and escape from dynamic cages within the contact layer and less so from weaker confinement along the $\hat{z}$ axis due to the liquid layering shown in Fig. 4.

3. *Influence of crystal facet, L/S interaction energy, and temperature on the self-intermediate scattering function within the contact layer*

In conventional glassy systems at equilibrium, the strength of 3D caging is typically extracted from the behavior of the self-intermediate scattering function. Here too we gain additional insight into the caging dynamics by evaluating $F_c^{\parallel}(\vec{k}_o, t)$ given by Eq. (12). The wave vector $\vec{k}_o$ denotes the set of RLVs corresponding to the maxima in the 2D structure factor in Fig. 9. For systems above the structural transition noted earlier, $\vec{k}_o$ coincides with the smallest (i.e primary) RLVs of the [011] facet; below the transition, $\vec{k}_o$ instead coincides with the second smallest RLVs. The significant jumps in Figs. 13(b) and 13(e) highlight the transition.

Only for the hotter layers against a [111] facet does the motion of particles exhibit a smooth, rapid, and direct transition from the ballistic to diffusive regime. In conventional systems consisting of a simple homogenous and isotropic bulk

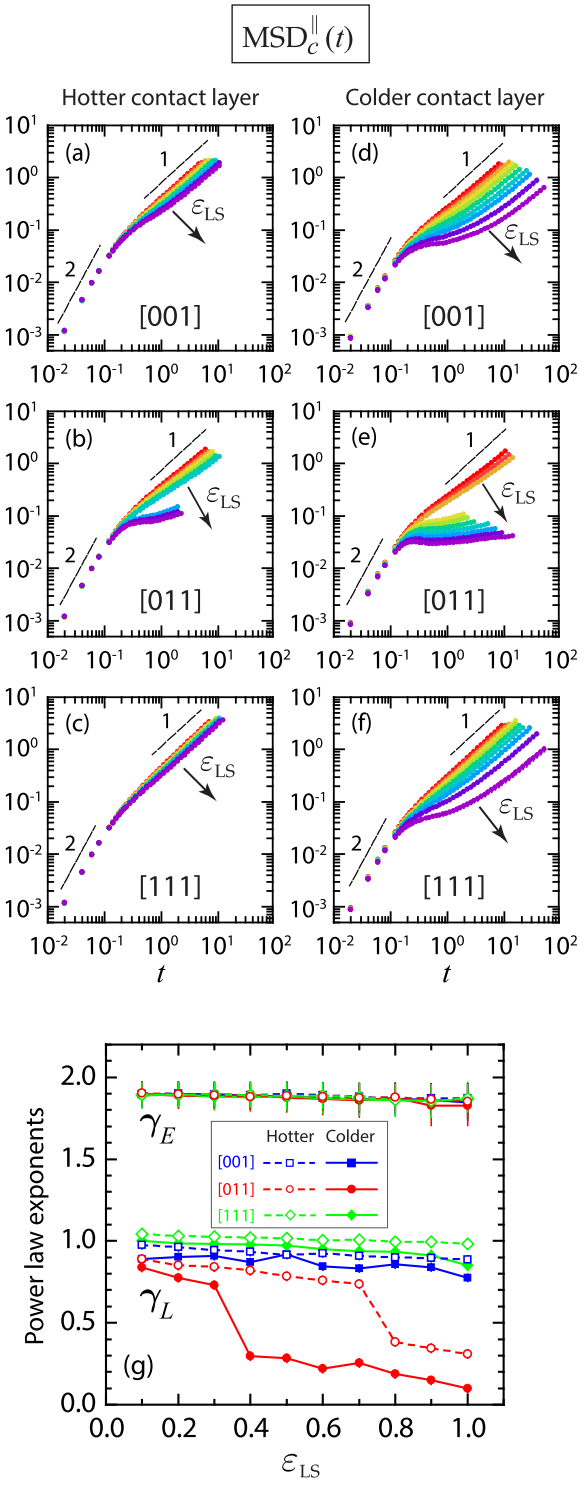

FIG. 11. (a)–(f) Mean-square displacement MSD$_c^{\parallel}(t)$ [Eq. (11)] for three facets and $0.1 \leqslant \varepsilon_{LS} \leqslant 1.0$ in increments of 0.1 for trajectories of ten or more particles which remained in the contact layer. Solid black lines are the exponents for a homogeneous isotropic bulk fluid. (g) Fitted exponents γ_E (strong superposition) and γ_L; connecting segments are a guide to the eye.

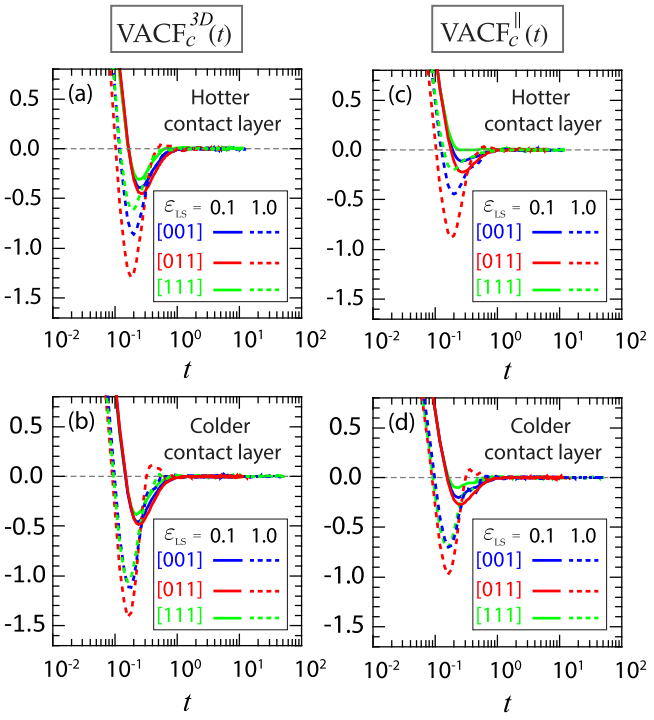

FIG. 12. Velocity autocorrelation function VACF$_c(t)$ [Eq. (13)] for three facet planes and $\varepsilon_{LS} = 0.1$ and 1.0 for trajectories of ten or more particles which remained in the contact layer. Superscripts 3D and $\parallel$ indicate evaluation of Eq. (13) based on 3D or 2D velocity vectors, respectively.

fluid, $F_c^{\parallel}(\vec{k}_o, t)$ decays rapidly to zero. Subsequent to the ballistic regime however, the results for all other systems shown in Fig. 13 exhibit some degree of caged motion or strong substrate induced localization such that $F_c^{\parallel}(\vec{k}_o, t)$ terminates at a nonzero value. In comparing results of the motion against the three facets at the same value of ε_{LS}, we see here too that the [011] facet induces the strongest degree of caged motion, as indicated by the relatively larger values of $F_c^{\parallel}(\vec{k}_o, t^*)$, similar to the behavior noted in Fig. 11. However, the duration of confinement is the shortest due to more rapid escape of particles from the contact layer. We also note that the colder layers against the [111] facet for the two largest values ε_{LS} exhibit an unusual signature marked by a prolonged decay with constant negative slope (on the linear-log axes). The rate and shape of decay is unlike the subdiffusive motion described above. The corresponding images in Fig. 8 and the 2D radial distribution profiles in Fig. 7 strongly suggest that these systems represent two cases of epitaxial locking with the crystal due to strong L/S bonding and colder temperature.

In equilibrium simulations of various glassy systems, the 3D self intermediate scattering function typically displays three distinct regimes: early time ballistic motion, intermediate caged motion, and late time diffusive motion. The entire span can usually be well fitted by a double stretched exponential represented by the Kohlrausch-Williams-Watt (KWW) function [66]. This function remains ever popular since the two time constants arising from the fit provide estimates of the average relaxation times associated with early ballistic and late time diffusive motion [67,68]. With the exception of the hotter contact layer against the [111] facet for the smallest values ε_{LS}, the majority of data in Fig. 13 could not be fitted

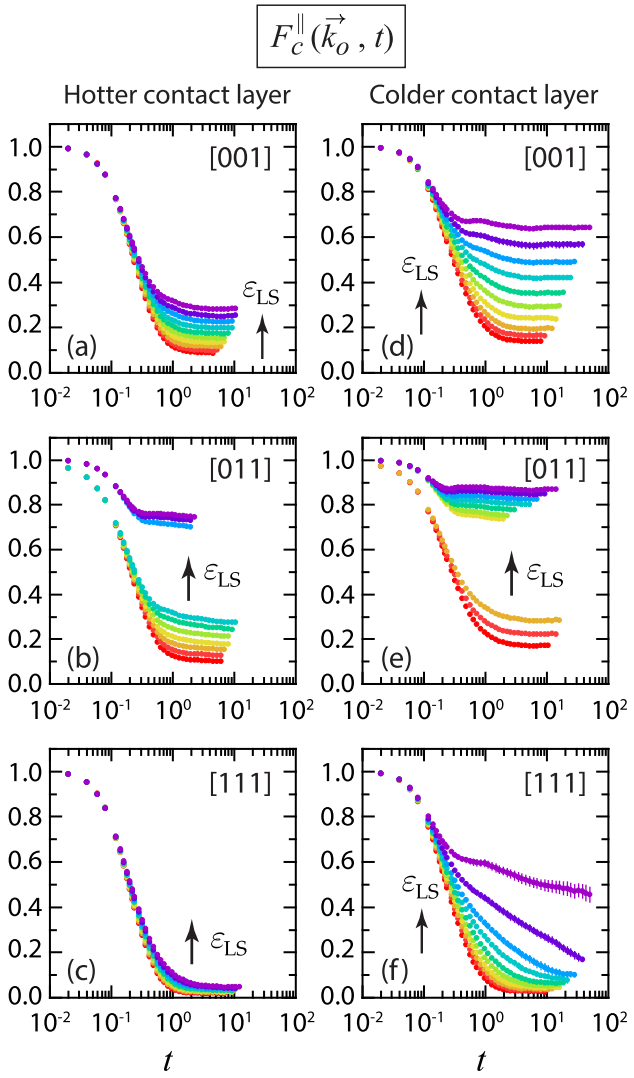

FIG. 13. (a)–(f) Self-intermediate scattering function $F_c^{\parallel}(\vec{k}_o, t)$ given by Eq. (12) for three facets and $0.1 \leqslant \varepsilon_{LS} \leqslant 1.0$ in increments of 0.1 for trajectories of ten or more particles which remained in the contact layer. Vertical lines through icons signify standard deviation which in some cases is not visible.

by a double exponential of KWW form spanning early to late times.

4. Influence of crystal facet, L/S interaction energy, and temperature on caging time and nonergodicity parameter within the contact layer

The plateaus in Fig. 13 are of significant interest since they signal an important transition from ergodic to nonergodic behavior [62,69,70]. For this reason, the magnitude of $F_c^{\parallel}(\vec{k}_o, t)$ in this regime is often called the nonergodicity parameter. Shown in Fig. 14 are the results for the average retention time t^* and the average nonergodicity parameter value $F^* = F_c^{\parallel}(\vec{k}_o, t^*)$ for the hotter and colder contact layers against three different facets with increasing ε_{LS}. The structural transition for the [011] case discussed earlier is quite evident in Figs. 14(a) and 14(b). For values of ε_{LS} above the

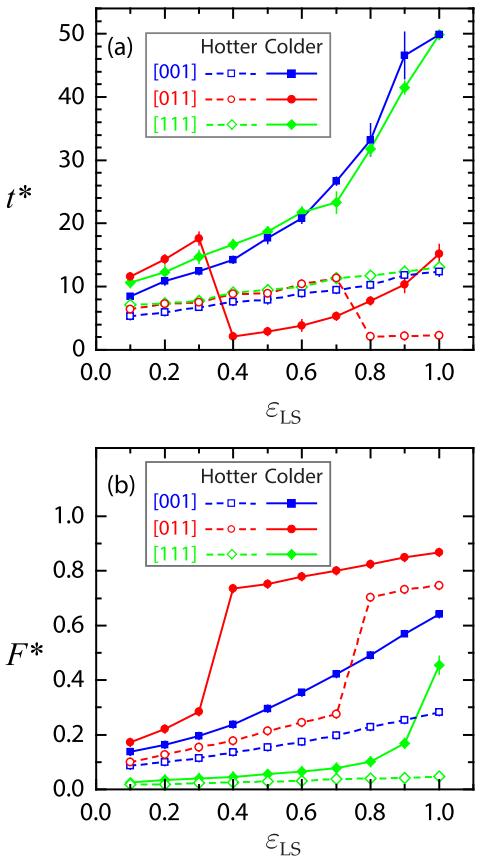

FIG. 14. (a) Retention time t^* and (b) corresponding value of the self-intermediate scattering function F^* extracted from the data in Fig. 13 for three facets and $0.1 \leqslant \varepsilon_{LS} \leqslant 1.0$ in increments of 0.1. Vertical lines through icons represent standard deviation; connecting segments are a guide to the eye.

structural transition, particles spend the least amount of time confined by 2D caged motion than similarly parameterized layers against the [001] or [111] facet. While the confinement time is shorter, however, the strength of confinement F^* is far larger. Below the structural transition incurred by the [011] facet, at similar layer temperature and identical value ε_{LS}, particles spend similar or slightly longer times experiencing subdiffusive or weakly caged motion as do the particles against the [001] and [111] facets, but again, the strength of confinement given by F^* is largest. As described in Sec. II C, the average retention time t^* was evaluated based on the occupancy constraint applied to the contact layer. A criterion based on a different number would yield different values t^* and F^* but a similar conclusion.

IV. ENHANCED THERMAL FLUX FROM ANISOTROPY OF L/S POTENTIAL LANDSCAPE

The discussion so far has centered on the special nature of the contact layer against the [011] facet. Next we try and relate 2D caged motion to the symmetry and structure of the underlying crystal lattice. For instance, the 2D Bravais lattice for the [011] facet has only twofold symmetry while the [001] facet has fourfold and the [111] facet sixfold symmetry. This reduced symmetry influences how the kinetic

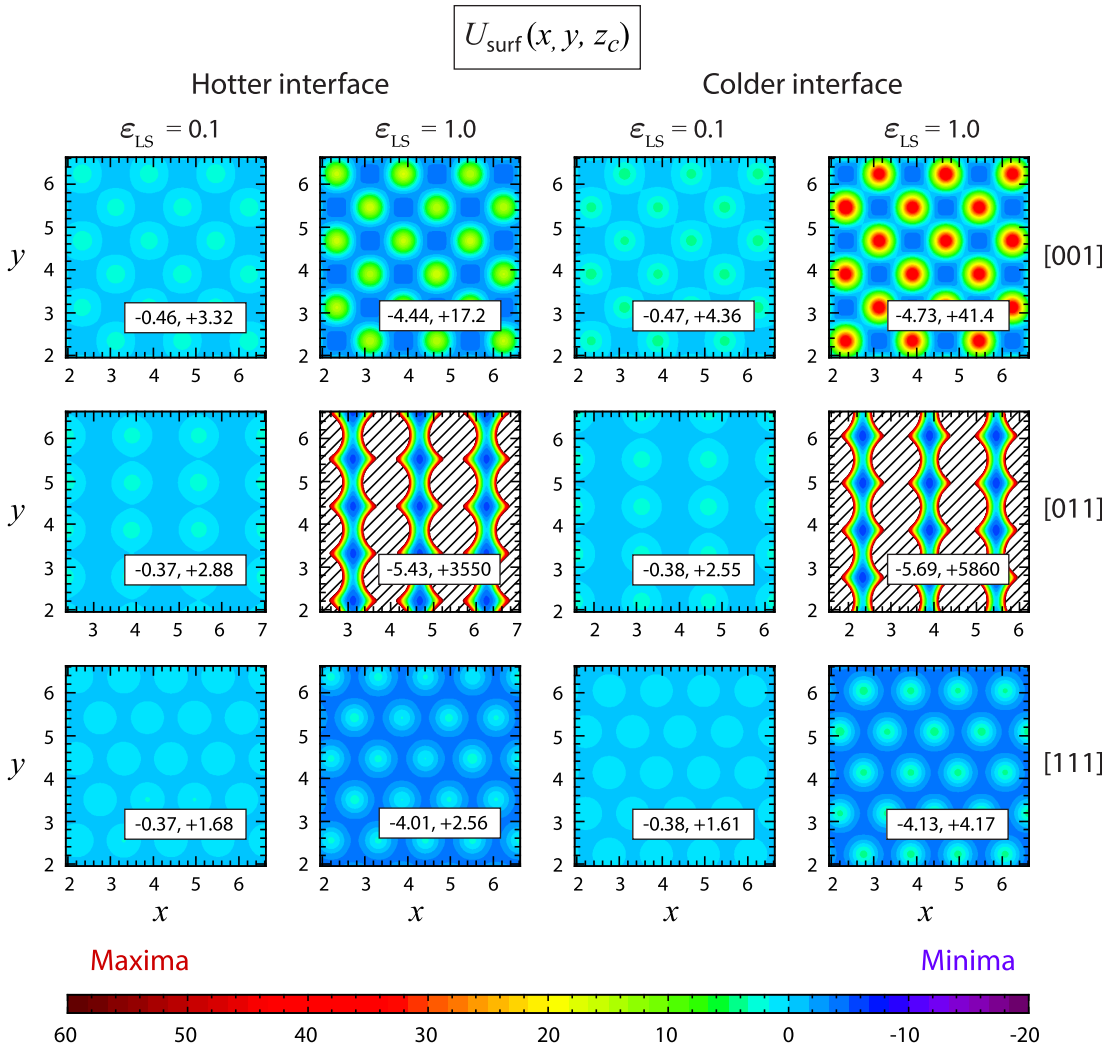

FIG. 15. Images of the L/S surface potential $U_{\text{surf}}(x, y, z_c)$ given by Eq. (17) acting on particles in the hotter and colder contact layers for three facet planes and $\varepsilon_{\text{LS}} = 0.1$ and 1.0. Numerical pairs indicated denote the minimum and maximum values of $U_{\text{surf}}(x, y, z_c)$ within the plaquette. Diagonal black lines lines indicate regions where $U_{\text{surf}} > 60$.

and potential energy of particles moving across these terrains partition differently along different Cartesian directions. Here, we examine some details of the L/S potential landscape for the smallest and largest values of ε_{LS}, which when evaluated together with the results in Figs. 11 and 13, highlight an additional special feature of the [011] facet.

Shown in Fig. 15 are images of the crystal surface potential given by

$$U_{\text{surf}}(x, y, z_c) = \left\langle \sum_{i=1}^{N_s} U_{\text{LS}}(|\vec{r}_c - \vec{r}_{s,i}|) \right\rangle \tag{17}$$

computed at the distance $z = z_c$ corresponding to the position of the peak in the liquid density ρ_c (see Fig. 4). Here, $\vec{r}_c = (x, y, z = z_c)$ denotes a coordinate in the contact layer, $\vec{r}_{s,i}$ is the coordinate of particle i in the solid layer, and N_s is the number of solid particles within the potential cutoff distance. The images represent a square plaquette with edge length of about three lattice constants centered in the $(\hat{x}, \hat{y})$ plane of the rectangular cell in Fig. 2(a). The plaquette was partitioned into a 200×200 array of smaller squares and measurements extracted from the grid center points.

The numerical values indicated in each panel represent the minimum and maximum values of $U_{\text{surf}}(x, y, z_c)$ within the plaquette. (Higher precision values with standard deviations are listed in Table X). The mean and standard deviation, based on 10^3 snapshots in time, were computed from the averaging scheme outlined in Sec. II B). Below we refer to the ratio of the maximum to minimum value as the max/min ratio.

For the examples shown in Fig. 15, at fixed value ε_{LS}, the minima of $U_{\text{surf}}(x, y, z_c)$ are all relatively insensitive to temperature; the maxima experience a small to large increase at colder temperatures depending on ε_{LS} and facet plane. This behavior accords with studies of the LJ potential which report that a decrease in temperature tends to cause a reduction in σ and increase in ε such that the repulsive contribution is more significant [71].

For $\varepsilon_{\text{LS}} = 0.1$, aside from the different symmetry, all the images are remarkably similar and show only a gentle

undulation in the potential landscape. This indicates a relatively smaller hindrance to particle motion inside the contact layer. This behavior, however, is not truly diffusive but subdiffusive [i.e., $\gamma_E < 1.0$ as shown in Fig. 11(g)], due to the influence of the crystal potential. For $\varepsilon_{LS} = 1.0$, the undulations in $U_{surf}(x, y, z_c)$ have larger amplitude and the slopes steepen further at colder temperatures. Here, the [011] case truly stands out in that its max/min ratio is about two and a half orders of magnitude larger than the rest for the hotter L/S interface and more than three orders of magnitude larger for the colder L/S interface. The [111] case has the smallest max/min ratio, which is why those particles exhibit the highest in-plane mobility in Fig. 11. The images of U_{surf} for the [011] facet also reveal that the tall repulsive barriers occupy a larger fraction of the area of the plaquette, which explains why the contact density ρ_c for the [011] case in Fig. 4(g) is the smallest of all three facet planes.

The strong anisotropy evident in the [011] potential surface for $\varepsilon_{LS} = 1.0$ leads to especially strong confinement of particles associated with 2D caged motion. In comparison to the other two cases, the [011] facet induces extremely large and rather wide repulsive barriers along the $\hat{x}$ axis and deeper attractive basins along the $\hat{y}$ axis. Consequently, motion along the $\hat{x}$ axis is strongly suppressed. The motion of particles along the $\hat{y}$ axis is also hindered since those channels are crowded by other liquid particles in the vicinity of the attractive basins. Given the resulting 2D caged motion, thermal fluctuations therefore tend to facilitate the escape of particles from the contact layer to the adjacent liquid layer much more readily. We also suspect that the trapping in 2D and rapid release into the third dimension allows more efficient transport of thermal energy along the $\hat{z}$ axis because of the highly correlated motion in the contact layer associated with the stringlike alignment.

V. CONCLUSION

It is often inferred from NEMD studies describing various influences on particle configuration in the first liquid layer near the solid surface that a higher contact density facilitates a higher L/S collision rate, leading to an enhancement in thermal exchange and a reduction in the thermal slip length. However, the counterexample presented here demonstrates why this is not always the case. The L/S systems examined demonstrate that under similar thermal conditions, the [011] facet above the structural transition maintains the smallest contact density yet engenders the highest thermal flux and smallest thermal slip length.

Results quantifying various structural and dynamic features of the contact layer reveal several distinguishing features responsible for the enhanced thermal tunneling. Liquid particles in the contact layer near the [011] facet plane adopt strong long-range order commensurate with the smallest reciprocal lattice vectors of the crystal surface. This commensurability is enhanced at lower temperature and stronger L/S bonding strength. The anisotropy of the corresponding L/S potential landscape causes a stringlike alignment of particles which effectively suppresses in-plane diffusion. The resulting 2D caged motion, quantified by the 2D mean-square displacement and 2D self-intermediate scattering function, is quite different than the type of caged motion observed in glassy systems. While this planar caging generates the largest values of the nonergodicity parameter, the corresponding caging times are shorter not longer, highlighting more rapid escape in the direction of the thermal flux. This type of trapping and release mechanism ultimately facilitates the highest thermal flux across the L/S interface with the smallest thermal slip length of the FCC facets examined. Given the fundamental nature of this investigation, we anticipate that the trapping and release mechanism demonstrated should extend more generally to many other L/S systems, especially those described by more complex interatomic potentials which incorporate harmonic, bond orientation, and/or Coulombic terms. If so, then mechanisms similar to the one outlined here can guide future design of L/S interfaces for maximizing thermal flux.

ACKNOWLEDGMENTS

H.K. and S.M.T. gratefully acknowledge financial support from a 2019 NASA Space Technology Graduate Research Fellowship (Grant No. 80NSSC19K1151) and the assistance of Dr. P. Thompson, who administers the computing cluster used in this study. S.M.T. also acknowledges an anonymous referee for the recommendation that the images in Fig. 15 be included in this work.

CREDIT AUTHOR STATEMENT

Conceptualization: S.M.T.; Data curation: S.M.T.; Formal analysis: H.K., S.M.T.; Funding acquisition: S.M.T.; Investigation: H.K., S.M.T.; Methodology: H.K., S.M.T.; Project administration: S.M.T.; Resources: S.M.T.; Software: H.K., S.M.T.; Supervision: S.M.T., A.I.B.; Validation: H.K., S.M.T.; Visualization: H.K., S.M.T.; Writing original draft: S.M.T.; Writing review & editing: S.M.T.

APPENDIX: TABULATED RESULTS

The tables in this Appendix contain information about the computational geometry in this paper and all measurements extracted from the NEMD simulations according to the methods described in Sec. II.

TABLE IV. Average number of particles $\langle N_c \rangle$ in the hotter and colder contact layers for different FCC facets and $\varepsilon_{LS} = 0.1$ and 1.0.

Facet	ε_{LS}	$\langle N_c \rangle_{hotter}$	$\langle N_c \rangle_{colder}$
[001]	0.1	104.3 ± 0.4	109.9 ± 0.4
[011]	0.1	116.6 ± 0.4	125.3 ± 0.4
[111]	0.1	122.0 ± 0.4	128.6 ± 0.4
[001]	1.0	114.9 ± 0.4	125.0 ± 0.5
[011]	1.0	80.7 ± 0.3	92.9 ± 0.4
[111]	1.0	134.1 ± 0.4	161.4 ± 0.5

TABLE V. Numerical results corresponding to the data in Fig. 5 for three FCC facets and ten values of the L/S interaction energy ε_{LS}. Listed are the mean and standard deviation (indicated in parentheses) values for the thermal flux J_z [Eq. (7)] and thermal gradient magnitude $|dT/dz|$ within the interior liquid and solid layers. Thermal conductivity values k computed from Eq. (2) are simply listed for reference and not required by the analysis.

			Liquid layer		Hotter solid layer		Colder solid layer	
Facet	ε_{LS}	$J_z \times 10^{-2}$	$\lvert dT/dz\rvert \times 10^{-2}$	k	$\lvert dT/dz\rvert \times 10^{-2}$	$k \times 10^{3}$	$\lvert dT/dz\rvert \times 10^{-2}$	$k \times 10^{3}$
[001]	0.1	6.88(0.05)	0.90(0.03)	7.63(0.26)	0.03(0.02)	0.24(0.09)	0.03(0.01)	0.32(0.20)
[001]	0.2	7.32(0.05)	0.98(0.03)	7.46(0.23)	0.04(0.02)	0.42(0.60)	0.03(0.01)	0.21(0.05)
[001]	0.3	7.93(0.11)	1.04(0.03)	7.63(0.31)	0.04(0.02)	0.24(0.24)	0.03(0.02)	0.35(0.19)
[001]	0.4	8.25(0.02)	1.10(0.03)	7.49(0.20)	0.05(0.02)	0.19(0.09)	0.04(0.01)	0.26(0.16)
[001]	0.5	8.63(0.03)	1.16(0.02)	7.45(0.11)	0.05(0.02)	0.30(0.30)	0.04(0.01)	0.24(0.11)
[001]	0.6	8.79(0.07)	1.19(0.03)	7.37(0.18)	0.05(0.01)	0.19(0.05)	0.04(0.01)	0.25(0.07)
[001]	0.7	9.33(0.03)	1.23(0.02)	7.57(0.09)	0.07(0.02)	0.14(0.04)	0.04(0.01)	0.24(0.06)
[001]	0.8	9.48(0.04)	1.29(0.02)	7.32(0.12)	0.05(0.02)	0.22(0.12)	0.03(0.01)	0.45(0.55)
[001]	0.9	9.70(0.04)	1.32(0.03)	7.38(0.15)	0.06(0.02)	0.18(0.06)	0.04(0.01)	0.28(0.10)
[001]	1.0	9.81(0.02)	1.35(0.03)	7.26(0.14)	0.05(0.02)	0.21(0.08)	0.04(0.01)	0.26(0.07)
[011]	0.1	7.71(0.03)	1.04(0.02)	7.39(0.13)	0.04(0.02)	0.53(1.03)	0.03(0.01)	0.25(0.06)
[011]	0.2	8.29(0.04)	1.10(0.02)	7.54(0.11)	0.05(0.02)	0.19(0.07)	0.03(0.01)	0.33(0.15)
[011]	0.3	8.92(0.06)	1.17(0.03)	7.64(0.14)	0.05(0.01)	0.18(0.04)	0.03(0.01)	0.40(0.24)
[011]	0.4	9.13(0.11)	1.22(0.01)	7.47(0.13)	0.06(0.02)	0.19(0.06)	0.04(0.01)	0.24(0.06)
[011]	0.5	9.51(0.04)	1.28(0.02)	7.43(0.17)	0.06(0.02)	0.17(0.05)	0.03(0.01)	0.35(0.16)
[011]	0.6	10.01(0.08)	1.32(0.02)	7.62(0.08)	0.06(0.01)	0.19(0.06)	0.04(0.01)	0.27(0.08)
[011]	0.7	10.07(0.08)	1.38(0.02)	7.26(0.14)	0.05(0.01)	0.22(0.06)	0.03(0.01)	0.39(0.25)
[011]	0.8	10.28(0.04)	1.41(0.04)	7.32(0.18)	0.05(0.02)	0.27(0.19)	0.03(0.01)	0.39(0.21)
[011]	0.9	10.63(0.03)	1.43(0.03)	7.40(0.13)	0.06(0.01)	0.20(0.04)	0.04(0.01)	0.30(0.11)
[011]	1.0	10.73(0.05)	1.46(0.02)	7.36(0.11)	0.05(0.02)	0.21(0.08)	0.04(0.01)	0.32(0.09)
[111]	0.1	7.05(0.04)	0.91(0.03)	7.72(0.28)	0.04(0.01)	0.20(0.09)	0.03(0.01)	0.23(0.09)
[111]	0.2	7.47(0.06)	0.99(0.03)	7.47(0.13)	0.04(0.02)	0.27(0.26)	0.03(0.01)	0.27(0.15)
[111]	0.3	8.14(0.02)	1.06(0.03)	7.68(0.20)	0.04(0.02)	0.24(0.12)	0.03(0.01)	0.34(0.16)
[111]	0.4	8.53(0.05)	1.13(0.01)	7.53(0.07)	0.04(0.01)	0.23(0.11)	0.03(0.01)	0.27(0.11)
[111]	0.5	8.88(0.03)	1.18(0.02)	7.56(0.13)	0.05(0.02)	0.19(0.10)	0.03(0.01)	0.26(0.07)
[111]	0.6	9.32(0.06)	1.23(0.03)	7.57(0.20)	0.06(0.01)	0.16(0.02)	0.03(0.02)	0.91(1.40)
[111]	0.7	9.64(0.07)	1.28(0.02)	7.55(0.13)	0.05(0.01)	0.19(0.05)	0.03(0.01)	0.28(0.08)
[111]	0.8	10.04(0.06)	1.33(0.02)	7.53(0.10)	0.05(0.02)	0.21(0.06)	0.04(0.01)	0.37(0.25)
[111]	0.9	10.22(0.03)	1.36(0.02)	7.49(0.10)	0.06(0.01)	0.20(0.05)	0.04(0.02)	0.29(0.12)
[111]	1.0	10.41(0.04)	1.40(0.02)	7.43(0.10)	0.05(0.03)	0.23(0.15)	0.04(0.01)	0.35(0.20)

TABLE VI. Numerical results in reduced units for the hotter and colder contact layers corresponding to the data in Figs. 6 and 9 for three FCC facets and ten values of L/S interaction energy ε_{LS}. Listed are the mean and standard deviations (indicated in parentheses) for the contact layer density ρ_c, maximum value of the static in-plane structure factor $S_{\max}$ [Eq. (10)], contact layer temperature T_c [Eq. (8)], thermal jump ΔT, and thermal slip length L_T [Eq. (3)].

		Hotter contact layer					Colder contact layer				
Facet	$\varepsilon_{\rm LS}$	ρ_c	$S_{\max}$	T_c	ΔT	L_T	ρ_c	$S_{\max}$	T_c	ΔT	L_T
[001]	0.1	1.351(0.013)	0.083(0.001)	1.451(0.008)	0.139(0.011)	15.457(1.616)	1.567(0.017)	0.124(0.003)	1.168(0.007)	0.155(0.009)	17.172(1.316)
[001]	0.2	1.455(0.029)	0.094(0.001)	1.461(0.007)	0.127(0.010)	12.942(1.279)	1.705(0.037)	0.148(0.002)	1.156(0.004)	0.140(0.006)	14.230(0.730)
[001]	0.3	1.535(0.036)	0.110(0.003)	1.471(0.009)	0.117(0.007)	11.231(0.967)	1.870(0.036)	0.181(0.002)	1.147(0.005)	0.129(0.006)	12.421(0.826)
[001]	0.4	1.629(0.010)	0.125(0.002)	1.475(0.005)	0.110(0.007)	9.975(0.833)	2.007(0.043)	0.222(0.003)	1.137(0.006)	0.116(0.007)	10.519(0.755)
[001]	0.5	1.699(0.024)	0.146(0.002)	1.486(0.006)	0.101(0.005)	8.748(0.568)	2.137(0.019)	0.272(0.004)	1.128(0.005)	0.104(0.003)	8.985(0.311)
[001]	0.6	1.790(0.021)	0.166(0.003)	1.491(0.004)	0.096(0.007)	8.077(0.740)	2.315(0.025)	0.335(0.004)	1.122(0.003)	0.101(0.004)	8.465(0.458)
[001]	0.7	1.869(0.029)	0.189(0.002)	1.492(0.005)	0.091(0.009)	7.461(0.829)	2.521(0.036)	0.403(0.004)	1.110(0.004)	0.089(0.005)	7.281(0.461)
[001]	0.8	1.957(0.030)	0.213(0.001)	1.501(0.004)	0.082(0.005)	6.316(0.488)	2.737(0.033)	0.486(0.004)	1.101(0.003)	0.080(0.005)	6.164(0.473)
[001]	0.9	2.042(0.021)	0.242(0.003)	1.506(0.009)	0.078(0.006)	5.955(0.560)	2.993(0.027)	0.567(0.005)	1.096(0.004)	0.074(0.003)	5.659(0.302)
[001]	1.0	2.126(0.034)	0.274(0.003)	1.513(0.004)	0.073(0.007)	5.362(0.580)	3.269(0.030)	0.645(0.006)	1.089(0.004)	0.069(0.006)	5.101(0.559)
[011]	0.1	0.963(0.021)	0.038(0.001)	1.470(0.006)	0.116(0.006)	11.175(0.607)	0.995(0.023)	0.036(0.001)	1.154(0.004)	0.135(0.007)	12.986(0.790)
[011]	0.2	0.980(0.016)	0.040(0.001)	1.475(0.008)	0.111(0.007)	10.157(0.757)	0.983(0.016)	0.037(0.000)	1.142(0.005)	0.124(0.005)	11.326(0.533)
[011]	0.3	0.970(0.018)	0.043(0.001)	1.484(0.007)	0.101(0.009)	8.697(0.950)	0.941(0.016)	0.040(0.001)	1.131(0.003)	0.113(0.004)	9.685(0.436)
[011]	0.4	0.961(0.017)	0.045(0.001)	1.493(0.003)	0.095(0.004)	7.810(0.354)	1.212(0.031)	0.552(0.002)	1.116(0.004)	0.096(0.003)	7.890(0.249)
[011]	0.5	0.945(0.022)	0.051(0.000)	1.498(0.006)	0.087(0.007)	6.817(0.627)	1.375(0.027)	0.588(0.004)	1.107(0.004)	0.086(0.006)	6.767(0.549)
[011]	0.6	1.006(0.013)	0.055(0.001)	1.506(0.005)	0.077(0.007)	5.860(0.579)	1.549(0.036)	0.651(0.003)	1.099(0.003)	0.082(0.004)	6.251(0.282)
[011]	0.7	1.077(0.027)	0.056(0.001)	1.514(0.004)	0.070(0.006)	5.057(0.493)	1.797(0.023)	0.713(0.003)	1.091(0.003)	0.070(0.004)	5.074(0.376)
[011]	0.8	1.164(0.025)	0.487(0.004)	1.521(0.008)	0.068(0.007)	4.824(0.594)	2.009(0.034)	0.768(0.003)	1.086(0.004)	0.065(0.006)	4.658(0.485)
[011]	0.9	1.253(0.015)	0.554(0.003)	1.526(0.005)	0.064(0.006)	4.485(0.489)	2.237(0.020)	0.814(0.003)	1.079(0.004)	0.058(0.004)	4.047(0.338)
[011]	1.0	1.329(0.013)	0.588(0.004)	1.529(0.006)	0.063(0.005)	4.285(0.378)	2.455(0.038)	0.851(0.003)	1.074(0.004)	0.051(0.005)	3.510(0.359)
[111]	0.1	1.525(0.017)	0.032(0.001)	1.445(0.007)	0.139(0.010)	15.208(1.579)	1.776(0.014)	0.042(0.001)	1.181(0.005)	0.164(0.005)	17.958(0.898)
[111]	0.2	1.664(0.022)	0.035(0.001)	1.452(0.009)	0.134(0.009)	13.498(1.314)	1.988(0.033)	0.048(0.001)	1.165(0.004)	0.145(0.006)	14.661(0.840)
[111]	0.3	1.781(0.026)	0.039(0.001)	1.459(0.008)	0.123(0.007)	11.660(0.878)	2.154(0.024)	0.055(0.002)	1.154(0.004)	0.134(0.006)	12.696(0.742)
[111]	0.4	1.876(0.026)	0.041(0.001)	1.470(0.008)	0.114(0.006)	10.089(0.661)	2.319(0.028)	0.065(0.002)	1.145(0.002)	0.121(0.004)	10.674(0.341)
[111]	0.5	1.989(0.022)	0.045(0.001)	1.475(0.006)	0.109(0.006)	9.260(0.657)	2.505(0.033)	0.076(0.002)	1.132(0.004)	0.110(0.004)	9.317(0.396)
[111]	0.6	2.091(0.027)	0.050(0.001)	1.486(0.006)	0.097(0.008)	7.921(0.745)	2.705(0.028)	0.093(0.002)	1.126(0.007)	0.105(0.005)	8.562(0.505)
[111]	0.7	2.165(0.020)	0.054(0.002)	1.488(0.005)	0.093(0.005)	7.255(0.455)	2.927(0.028)	0.117(0.005)	1.116(0.004)	0.094(0.004)	7.380(0.415)
[111]	0.8	2.260(0.029)	0.059(0.001)	1.498(0.006)	0.086(0.005)	6.418(0.404)	3.171(0.040)	0.159(0.005)	1.110(0.004)	0.086(0.005)	6.455(0.469)
[111]	0.9	2.403(0.018)	0.063(0.001)	1.496(0.005)	0.082(0.003)	6.051(0.315)	3.439(0.035)	0.290(0.033)	1.100(0.004)	0.078(0.004)	5.763(0.374)
[111]	1.0	2.490(0.028)	0.070(0.001)	1.503(0.007)	0.078(0.006)	5.534(0.447)	3.812(0.039)	0.582(0.018)	1.095(0.004)	0.071(0.006)	5.093(0.461)

TABLE VII. Coefficients a, b and c from least-squares fits to Eq. (15).

Facet	H/C side	a	b	c
[001]	H	16.5 ± 0.5	19.0 ± 2.0	8.0 ± 1.0
[011]	H	12.9 ± 0.2	15.9 ± 0.8	7.3 ± 0.6
[111]	H	16.9 ± 0.3	20.0 ± 1.0	8.7 ± 0.8
[001]	C	18.7 ± 0.6	24.0 ± 2.0	11.0 ± 2.0
[011]	C	14.7 ± 0.5	20.0 ± 2.0	9.0 ± 1.0
[111]	C	19.5 ± 0.6	26.0 ± 2.0	12.0 ± 2.0

TABLE VIII. Coefficients α_1 and α_2 from least-squares fits to Eq. (16).

Facet	H/C side	α_1	α_2
[001]	H	11.8 ± 0.4	0.88 ± 0.04
[011]	H	8.40 ± 1.0	0.17 ± 0.12
[111]	H	14.2 ± 0.3	1.00 ± 0.02
[001]	C	6.60 ± 0.2	0.94 ± 0.02
[011]	C	2.70 ± 0.9	0.63 ± 0.12
[111]	C	8.03 ± 0.4	1.03 ± 0.04

TABLE IX. Numerical results in reduced units for the hotter and colder contact layers corresponding to the data in Figs. 11 and 14 for three FCC facets and ten values of L/S interaction energy $\varepsilon_{\mathrm{LS}}$. Listed are the measured exponents γ_E and γ_L from least-squares fits to the 2D mean-square displacement curves in Fig. 11; parentheses signify 95% confidence intervals. Also listed are the mean and standard deviations (in parentheses) of the nonergodicity parameter $F_c^*(\vec{k}_o)$ [Eq. (12)] at the retention time t^*.

		Hotter contact layer				Colder contact layer			
Facet	ε_{LS}	γ_E	γ_L	F^*	t^*	γ_E	γ_L	F^*	t^*
[001]	0.1	1.8969(0.0733)	0.9745(0.0010)	0.0861(0.0047)	5.3100(0.3100)	1.8932(0.0758)	0.8897(0.0022)	0.1375(0.0004)	8.4500(0.5400)
[001]	0.2	1.9017(0.0689)	0.9626(0.0012)	0.0991(0.0029)	5.9400(0.2946)	1.8984(0.0694)	0.9022(0.0018)	0.1631(0.0033)	10.8467(0.5900)
[001]	0.3	1.8952(0.0722)	0.9434(0.0020)	0.1146(0.0006)	6.7100(0.5220)	1.8958(0.0744)	0.9082(0.0018)	0.1953(0.0043)	12.4067(0.3921)
[001]	0.4	1.8899(0.0772)	0.9340(0.0014)	0.1364(0.0004)	7.5800(0.1970)	1.8867(0.0777)	0.8700(0.0024)	0.2379(0.0064)	14.2200(0.1058)
[001]	0.5	1.8990(0.0722)	0.9150(0.0022)	0.1549(0.0010)	7.8700(0.5910)	1.8846(0.0816)	0.9173(0.0020)	0.2959(0.0072)	17.7067(0.8429)
[001]	0.6	1.8912(0.0747)	0.9260(0.0020)	0.1732(0.0025)	8.9600(0.2553)	1.8731(0.0875)	0.8442(0.0020)	0.3542(0.0016)	20.8067(0.7814)
[001]	0.7	1.8801(0.0813)	0.9095(0.0022)	0.1969(0.0044)	9.4800(0.1970)	1.8646(0.0958)	0.8322(0.0024)	0.4213(0.0059)	26.6933(0.6395)
[001]	0.8	1.8700(0.0872)	0.8977(0.0020)	0.2277(0.0026)	10.2800(0.4854)	1.8674(0.0972)	0.8568(0.0020)	0.4901(0.0059)	33.2133(2.5694)
[001]	0.9	1.8727(0.0886)	0.8966(0.0020)	0.2540(0.0018)	11.8200(0.4652)	1.8607(0.1000)	0.8386(0.0020)	0.5681(0.0117)	46.5600(3.6550)
[001]	1.0	1.8715(0.0888)	0.8865(0.0022)	0.2832(0.0063)	12.3267(0.6906)	1.8458(0.1077)	0.7743(0.0025)	0.6410(0.0038)	49.8400(0.0000)
[011]	0.1	1.9025(0.0672)	0.8894(0.0006)	0.0994(0.0036)	6.4300(0.4050)	1.8962(0.0739)	0.8394(0.0016)	0.1713(0.0031)	11.5933(0.5201)
[011]	0.2	1.8963(0.0727)	0.8509(0.0006)	0.1274(0.0016)	7.3133(0.5637)	1.8889(0.0783)	0.7756(0.0016)	0.2216(0.0046)	14.3000(0.7158)
[011]	0.3	1.8894(0.0764)	0.8413(0.0010)	0.1537(0.0019)	7.5133(0.3743)	1.8854(0.0772)	0.7304(0.0014)	0.2846(0.0022)	17.5800(1.0153)
[011]	0.4	1.8826(0.0805)	0.8192(0.0016)	0.1780(0.0034)	8.8333(0.5201)	1.8935(0.0758)	0.2980(0.0062)	0.7358(0.0029)	2.0867(0.1332)
[011]	0.5	1.8870(0.0775)	0.7858(0.0020)	0.2139(0.0060)	8.9067(0.6438)	1.8760(0.0888)	0.2826(0.0030)	0.7520(0.0016)	2.9000(0.5724)
[011]	0.6	1.8810(0.0811)	0.7585(0.0022)	0.2439(0.0051)	10.3733(0.4086)	1.8682(0.0947)	0.2203(0.0032)	0.7783(0.0025)	3.8400(0.9007)
[011]	0.7	1.8760(0.0872)	0.7375(0.0028)	0.2751(0.0043)	11.3133(0.4801)	1.8592(0.1011)	0.2544(0.0028)	0.8010(0.0016)	5.3000(0.1217)
[011]	0.8	1.8769(0.0866)	0.3829(0.0080)	0.7021(0.0022)	2.1067(0.1137)	1.8748(0.0869)	0.1889(0.0006)	0.8242(0.0018)	7.7867(0.3252)
[011]	0.9	1.8654(0.0925)	0.3438(0.0062)	0.7318(0.0023)	2.1933(0.1943)	1.8275(0.1202)	0.1494(0.0014)	0.8488(0.0014)	10.2933(1.1856)
[011]	1.0	1.8536(0.1038)	0.3101(0.0048)	0.7459(0.0030)	2.2500(0.1700)	1.8276(0.1233)	0.0978(0.0016)	0.8679(0.0009)	15.2000(1.4500)
[111]	0.1	1.8930(0.0750)	1.0431(0.0008)	0.0184(0.0039)	7.1500(0.2420)	1.8881(0.0777)	1.0005(0.0004)	0.0249(0.0008)	10.6000(0.4550)
[111]	0.2	1.8953(0.0722)	1.0307(0.0008)	0.0186(0.0024)	7.3667(0.3139)	1.8980(0.0730)	0.9841(0.0004)	0.0347(0.0061)	12.2533(1.0191)
[111]	0.3	1.8960(0.0727)	1.0266(0.0008)	0.0233(0.0006)	7.7900(0.6510)	1.8821(0.0819)	0.9836(0.0006)	0.0391(0.0017)	14.7333(1.0108)
[111]	0.4	1.8923(0.0736)	1.0206(0.0008)	0.0248(0.0006)	9.0500(0.0611)	1.8784(0.0861)	0.9783(0.0008)	0.0449(0.0033)	16.6333(0.1677)
[111]	0.5	1.8870(0.0761)	1.0182(0.0010)	0.0288(0.0010)	9.5100(0.4130)	1.8834(0.0819)	0.9726(0.0006)	0.0555(0.0012)	18.7067(0.5601)
[111]	0.6	1.8876(0.0755)	1.0048(0.0010)	0.0310(0.0012)	9.9667(0.5132)	1.8711(0.0883)	0.9492(0.0008)	0.0648(0.0023)	21.7600(0.8681)
[111]	0.7	1.8806(0.0833)	1.0064(0.0004)	0.0384(0.0018)	11.3667(0.4272)	1.8641(0.0941)	0.9370(0.0010)	0.0783(0.0119)	23.3200(1.6837)
[111]	0.8	1.8619(0.0938)	0.9932(0.0006)	0.0399(0.0040)	11.7467(0.7829)	1.8603(0.1000)	0.9343(0.0010)	0.1011(0.0082)	31.7733(1.0801)
[111]	0.9	1.8551(0.0988)	0.9949(0.0006)	0.0411(0.0044)	12.4000(0.8492)	1.8587(0.1025)	0.9128(0.0008)	0.1689(0.0098)	41.4600(1.0054)
[111]	1.0	1.8712(0.0838)	0.9824(0.0006)	0.0473(0.0035)	13.0600(0.6879)	1.8609(0.1102)	0.8528(0.0014)	0.4551(0.0323)	49.8600(0.0000)

TABLE X. Minimum and maximum values of the crystal surface potential U_{surf} computed from Eq. (17) for the plaquettes shown in Fig. 15.

Facet	H/C side	ε_{LS}	Min	Max
[001]	H	0.1	−0.455 (0.001)	3.32 (0.20)
[001]	C	0.1	−0.472 (0.001)	4.36 (0.19)
[001]	H	1.0	−4.435 (0.010)	17.2 (0.63)
[001]	C	1.0	−4.727 (0.004)	41.4 (1.54)
[011]	H	0.1	−0.373 (0.002)	2.88 (0.68)
[011]	C	0.1	−0.382 (0.001)	2.55 (0.06)
[011]	H	1.0	−5.425 (0.021)	3550 (497)
[011]	C	1.0	−5.688 (0.016)	5860 (172)
[111]	H	0.1	−0.367 (0.003)	1.68 (0.09)
[111]	C	0.1	−0.380 (0.002)	1.61 (0.04)
[111]	H	1.0	−4.011 (0.010)	2.56 (0.24)
[111]	C	1.0	−4.127 (0.004)	4.17 (0.16)

[1] M. Kimball, The AI craze is highlighting the cooling crunch, Forbes, 20 Feb. 2024, https://www.forbes.com/sites/moorinsights/2024/02/20/ the-ai-craze-is-highlighting-the-cooling-crunch/?sh=609ab8592678.

[2] S. Rangarajan, S. N. Schiffres, and B. Sammakia, A review of recent developments in "on-chip" embedded cooling technologies for heterogeneous integrated applications, Engineering **26**, 185 (2023).

[3] R. van Erp, R. Soleimanzadeh, L. Nela, G. Kampitsis, and E. Matioli, Co-designing electronics with microfluidics for more sustainable cooling, Nature (London) **585**, 211 (2020).

[4] T. Endo, A. Nukada, and S. Matsuoka, TSUBAME-KFC: A modern liquid submersion cooling prototype towards exascale becoming the greenest supercomputer in the world, in *2014 20th IEEE International Conference on Parallel and Distributed Systems (ICPADS)* (IEEE, Hsinchu, Taiwan, 2021), pp. 360–367.

[5] T. Endo, A. Nukada, and S. Matsuoka, Cost–efficient overclocking in immersion-cooled datacenters, in *48th Annual International Symposium on Computer Architecture (ISCA)* (ACM/IEEE, Valencia, Spain, 2021), pp. 623–636.

[6] G. Rak, IBM demos transistor built for liquid nitrogen cooling, https://spectrum.ieee.org/nanosheet-transistor (2023).

[7] P. L. Kapitza, Heat transfer and superfluidity of Helium II, Phys. Rev. **60**, 354 (1941).

[8] R. J. Warzoha, A. A. Wilson, B. F. Donovan, A. Clark, X. Cheng, L. An, E. Lee, X. Liu, and G. Feng, Confined transducer geometries to enhance sensitivity to thermal boundary conductance in frequency–domain thermoreflectance measurements, in *ASME 2021 International Technical Conference and Exhibition on Packaging and Integration of Electronic and Photonic Microsystems* (ASME, 2021), pp. IPACK2021–66842.

[9] K. Yu, R. Enright, and D. McCloskey, Quantifying interfacial thermal conductance at solid–liquid interfaces using frequency-domain thermoreflectance and analytical methods, in *21st IEEE Intersociety Conference on Thermal and Thermomechanical Phenomena in Electronic Systems (iTherm)* (IEEE, San Diego, CA, 2022), pp. 1–6.

[10] N. Shenogina, R. Godawat, P. Keblinski, and S. Garde, How wetting and adhesion affect thermal conductance of a range of hydrophobic to hydrophilic aqueous interfaces, Phys. Rev. Lett. **102**, 156101 (2009).

[11] E. Helfand and S. A. Rice, Principle of corresponding states for transport properties, J. Chem. Phys. **32**, 1642 (1960).

[12] K. Kanhaiya, S. Kim, W. Im, and H. Heinz, Accurate simulation of surfaces and interfaces of ten FCC metals and steel using Lennard–Jones potentials, npj Comput. Mater. **7**, 17 (2021).

[13] A. Tenenbaum, G. Ciccotti, and R. Gallico, Stationary nonequilibrium states by molecular dynamics. Fourier's law, Phys. Rev. A **25**, 2778 (1982).

[14] S. Matsumoto, Molecular dynamics simulation of a liquid droplet on a solid surface, J. Jpn. Soc. Tribol. **42**, 93 (1997).

[15] S. Maruyama, T. Kurashige, S. Matsumoto, Y. Yamaguchi, and T. Kimura, Liquid droplet in contact with a solid surface, Micro. Thermophys. Eng. **2**, 49 (1998).

[16] S. Maruyama and T. Kimura, A study on thermal resistance over a solid–liquid interface by the molecular dynamics method, Thermal Sci. Eng. **7**, 63 (1999).

[17] J.-L. Barrat and F. Chiaruttini, Kapitza resistance at the liquid–solid interface, Mol. Phys. **101**, 1605 (2003).

[18] L. Xue, P. Keblinski, S. R. Phillpot, S. U.-S. Choi, and J. A. Eastman, Two regimes of thermal resistance at a liquid–solid interface, J. Chem. Phys. **118**, 337 (2003).

[19] L. Xue, P. Keblinski, S. R. Phillpot, S. U.-S. Choi, and J. A. Eastman, Effect of liquid layering at the liquid–solid interface on thermal transport, Int. J. Mech. Sci. **47**, 4277 (2004).

[20] Y. Wang and P. Keblinski, Role of wetting and nanoscale roughness on thermal conductance at liquid–solid interface, Appl. Phys. Lett. **99**, 073112 (2011).

[21] S. Murad and I. K. Puri, Thermal transport across nanoscale solid–fluid interfaces, Appl. Phys. Lett. **92**, 133105 (2008).

[22] H. Han, S. Mérabia, and F. Müller-Plathe, Thermal transport at solid–liquid interfaces: High pressure facilitates heat flow through nonlocal liquid structuring, J. Phys. Chem. Lett. **8**, 1946 (2017).

[23] G. Balasubramanian, S. Banerjee, and I. K. Puri, Unsteady nanoscale thermal transport across a solid–fluid interface, J. Appl. Phys. **104**, 064306 (2008).

[24] A. K. M. M. Morshed, T. Paul, and J. A. Khan, Atomistic simulation of temperature dependent thermal transport across nanoconfined liquid, Physica E **47**, 246 (2013).

[25] T. Ohara and D. Torii, Molecular dynamics study of thermal phenomena in an ultrathin liquid film sheared between solid surfaces: The influence of the crystal plane on energy and momentum transfer at solid-liquid interfaces, J. Chem. Phys. **122**, 214717 (2005).

[26] D. Torii, T. Ohara, and K. Ishida, Molecular-scale mechanism of thermal resistance at the solid–liquid interfaces: Influence of interaction parameters between solid and liquid molecules, J. Heat Transfer **132**, 012402 (2010).

[27] B. H. Kim, A. Beskok, and T. Cagin, Molecular dynamics simulations of thermal resistance at the liquid-solid interface, J. Chem. Phys. **129**, 174701 (2008).

[28] Z. Liang and H.-L. Tsai, Effect of molecular film thickness on thermal conduction across solid-film interfaces, Phys. Rev. E **83**, 061603 (2011).

[29] S. Alosious, S. K. Kannam, S. P. Sethian, and B. D. Todd, Prediction of Kapitza resistance at fluid–solid interfaces, J. Chem. Phys. **151**, 194502 (2019).

[30] S. A. Somers and H. T. Davis, Microscopic dynamics of fluids confined between smooth and atomically structured solid surfaces, J. Chem. Phys. **96**, 5389 (1992).

[31] J. R. Henderson and F. van Swol, On the interface between a fluid and a planar wall: Theory and simulations of a hard sphere fluid at a hard wall, Mol. Phys. **51**, 991 (1984).

[32] J. Gao, W. D. Luedtke, and U. Landman, Layering transitions and dynamics of confined liquid films, Phys. Rev. Lett. **79**, 705 (1997).

[33] S. Murad and I. K. Puri, Molecular simulation of thermal transport across hydrophilic interfaces, Chem. Phys. Lett. **467**, 110 (2008).

[34] A. Pham, M. Barisik, and B. Kim, Pressure dependence of Kapitza resistance at gold/water and silicon/water interfaces, J. Chem. Phys. **139**, 244702 (2013).

[35] G. Song and C. Min, Temperature dependence of thermal resistance at a solid/liquid interface, Mol. Phys. **111**, 903 (2013).

[36] S. W. Hung, G. Kikugawa, and J. Shiomi, Mechanism of temperature dependent thermal transport across the interface between self-assembled monolayer and water, J. Phys. Chem. C **120**, 26678 (2016).

[37] B. Ramos-Alvarado, S. Kumar, and G. P. Peterson, Solid–liquid thermal transport and its relationship with wettability and the interfacial liquid structure, J. Phys. Chem. Lett. **7**, 3497 (2016).

[38] A. Michels, H. Wijker, and H. Wijker, Isotherms of argon between 0° C and 150° C and pressures up to 2900 atmospheres, Physica **15**, 627 (1949).

[39] L. Verlet, Computer "experiments" on classical fluids. I. Thermodynamical properties of Lennard-Jones molecules, Phys. Rev. **159**, 98 (1967).

[40] B. L. Holian and D. J. Evans, Shear viscosities away from the melting line: A comparison of equilibrium and nonequilibrium molecular dynamics, J. Chem. Phys. **78**, 5147 (1983).

[41] M. Cieplak, J. Koplik, and J. R. Banavar, Boundary conditions at a fluid–solid interface, Phys. Rev. Lett. **86**, 803 (2001).

[42] R. J. Stevens, L. V. Zhigilei, and P. M. Norris, Effects of temperature and disorder on thermal boundary conductance at solid–solid interfaces: Nonequilibrium molecular dynamics simulations, Int. J. Mech. Sci. **50**, 3977 (2007).

[43] S. Plimpton, Fast parallel algorithms for short–range molecular dynamics, J. Comput. Phys. **117**, 1 (1995).

[44] A. P. Thompson, H. M. Aktulga, R. Berger, D. S. Bolintineanu, W. M. Brown, P. S. Crozier, P. J. in 't Veld, A. Kohlmeyer, S. G. Moore, T. D. Nguyen, R. Shan, M. J. Stevens, J. Tranchida, C. Trott, and S. J. Plimpton, LAMMPS – A flexible simulation tool for particle–based materials modeling at the atomic, meso, and continuum scales, Comput. Phys. Commun. **271**, 108171 (2022).

[45] W. G. Hoover, Canonical dynamics: Equilibrium phase–space distributions, Phys. Rev. A **31**, 1695 (1985).

[46] T. Schneider and E. Stoll, Molecular–dynamics study of a three–dimensional one–component model for distortive phase transitions, Phys. Rev. B **17**, 1302 (1978).

[47] M. Thol, G. Rutkai, A. Köster, R. Lustig, R. Span, and J. Vrabec, Equation of state for the Lennard-Jones fluid, J. Phys. Chem. Ref. Data **45**, 023101 (2016).

[48] Z. Liang and P. Keblinski, Finite–size effects on molecular dynamics interfacial thermal–resistance predictions, Phys. Rev. B **90**, 075411 (2014).

[49] In studies of L/S systems, the structure factor is often computed from the relation $|\sum_i^{N_c} \exp(-i\boldsymbol{k}\cdot\boldsymbol{r}_i)|^2$ instead of Eq. (10). The quadratic relation, however, is strictly valid only for liquid particles situated on the sites of a Bravais lattice.

[50] S. Toxvaerd, The structure and thermodynamics of a solid–fluid interface, J. Chem. Phys. **74**, 1998 (1981).

[51] E. Velasco and P. Tarazona, Phase transitions at solid–fluid interfaces: Theoretical description of the transverse structure, Surf. Sci. **251–252**, 628 (1991).

[52] P. A. Thompson and M. O. Robbins, Shear flow near solids: Epitaxial rrder and flow boundary conditions, Phys. Rev. A **41**, 6830 (1990).

[53] B. D. Todd and D. J. Evans, The heat flux vector for highly inhomogeneous nonequilibrium fluids in very narrow pores, J. Chem. Phys. **103**, 9804 (1995).

[54] N. V. Priezjev, A. A. Darhuber, and S. M. Troian, Slip behavior in liquid films on surfaces of patterned wettability: Comparison between continuum and molecular dynamics, Phys. Rev. E **71**, 041608 (2005).

[55] M. Barisik and A. Beskok, Temperature dependence of thermal resistance at the water/silicon interface, Int. J. Therm. Sci. **77**, 47 (2014).

[56] G. L. Pollack, Kapitza resistance, Rev. Mod. Phys. **41**, 48 (1969).

[57] I. M. Khalatnikov, *An Introduction to the Theory of Superfludity* (CRC Press, Taylor & Francis, Boca Raton, FL, 2018), English translation of Russian edition by P. C. Hohenberg.

[58] P. Langevin, Sur la théorie du mouvement Brownien, C. R. Acad. Sci. Paris **146**, 530 (1908).

[59] V. Vladimirsky and Y. A. Terletzky, Hydrodynamical theory of translational Brownian motion, Zh. Eksp. Teor. Fiz. **15**, 258 (1945).

[60] E. J. Hinch, Application of the Langevin equation to fluid suspensions, J. Fluid Mech. **72**, 499 (1975).

[61] M. Fuchs, W. Götze, and M. R. Mayr, Asymptotic laws for tagged-particle motion in glassy systems, Phys. Rev. E **58**, 3384 (1998).

[62] W. Kob and H. C. Andersen, Scaling behavior in the β–relaxation regime of a supercooled Lennard-Jones mixture, Phys. Rev. Lett. **73**, 1376 (1994).

[63] W. Kob, Computer simulations of supercooled liquids and glasses, J. Phys.: Condens. Matter **11**, R85 (1999).

[64] D. P. Dean and J. N. Kushick, On the role of attractive forces in the cage effect in simple liquids, J. Chem. Phys. **76**, 619 (1982).

[65] Y. Endo and H. Endo, Microscopic mechanism of the cage effect in simple liquids, Phys. Lett. A **95**, 92 (1983).

[66] J. Phillips, Stretched exponential relaxation in molecular and electronic glasses, Rep. Prog. Phys. **59**, 1133 (1996).

[67] W. Zhang, J. F. Douglas, and F. W. Starr, Effects of a "bound" substrate layer on the dynamics of supported polymer films, J. Chem. Phys. **147**, 044901 (2017).

[68] R. Higler, J. Krausser, J. van der Gucht, A. Zaccone, and J. Sprakel, Linking slow dynamics and microscopic connectivity in dense suspensions of charged colloids, Soft Matter **14**, 780 (2018).

[69] G. Wahnström, Molecular–dynamics study of a supercooled two-component Lennard–Jones system, Phys. Rev. A **44**, 3752 (1991).

[70] R. D. Mountain and D. Thirumalai, Relationship between the fluctuation metric and the non-ergodicity parameter: Incoherent scattering function, Physica A **192**, 543 (1993).

[71] G. Parsafar, F. Kermanpour, and B. Najafi, Prediction of the temperature and density dependencies of the parameters of the average effective pair potential using only the LIR equation of state, J. Phys. Chem. B **103**, 7287 (1999).